

Electronic Thesis and Dissertation Repository

8-17-2016 12:00 AM

Self-assembled copper nanoparticle superlattices on graphene thin films

Tianhao Ouyang
The University of Western Ontario

Supervisor
Giovanni Fanchini
The University of Western Ontario Joint Supervisor

Michael G. Cottam
The University of Western Ontario

Graduate Program in Physics

A thesis submitted in partial fulfillment of the requirements for the degree in Master of Science
© Tianhao Ouyang 2016

Follow this and additional works at: <https://ir.lib.uwo.ca/etd>

 Part of the [Condensed Matter Physics Commons](#)

Recommended Citation

Ouyang, Tianhao, "Self-assembled copper nanoparticle superlattices on graphene thin films" (2016).
Electronic Thesis and Dissertation Repository. 3940.
<https://ir.lib.uwo.ca/etd/3940>

This Dissertation/Thesis is brought to you for free and open access by Scholarship@Western. It has been accepted for inclusion in Electronic Thesis and Dissertation Repository by an authorized administrator of Scholarship@Western. For more information, please contact wlsadmin@uwo.ca.

Abstract

Recently, Giovannetti *et al.* successfully demonstrated that some metals (such as Cu and Au) only have weak van der Waals interaction with graphene and thus can only form weak bonding without severely shifting graphene's band structure, which describes the energy range of the electrons in the material. Therefore, this opens up windows for graphene enhancement without greatly changing its properties. Furthermore, Zhou *et al.* later suggested the possibility of self-assembling periodic arrays of alkali atoms on graphene. In our group, graphene thin films fabricated in a cost-effective way using solution-processed methods have been used extensively, including decorating graphene thin films with metallic nanoparticles for optical enhancement. Motivated by these experiments, our study reports a facile fabrication method for copper nanoparticle (Cu-np) superlattice, which is a periodic structure of copper-nanoparticle lines. This fabrication is based on thermal evaporation of ultrathin layers of copper. These copper layers are deposited on solution-processed thin films formed by few-layer graphene platelets. We show that the annealing of these systems in nitrogen without previous exposure to air prompts the heterogeneous nucleation of the Cu layer into nanoparticle superlattices. And these nanoparticles self-assemble along specific crystallographic directions of graphene. Theoretical calculations suggest the lowest formation energy for Cu-nanoparticle arrays forming along armchair directions, indicating that their self-assembly is energetically more favorable. The possibility of using these superlattices in evanescent waveguiding devices is explored by scanning near-field optical microscopy. The light-confining properties of our systems in the near field indicate that our nanoparticle superlattices are poised to satisfy the technological demands required by nanophotonics devices.

Keywords: solution-prepared graphene thin films; thermal evaporated copper nanoparticle, self-assembly; spontaneous formation; superlattices; tight-binding model; evanescent waveguide

Co-Authorship Statement

This thesis is partially based on a published paper “self-assembly metallic nanoparticle superlattices on large-area graphene thin films: growth and evanescent waveguiding properties”, *RSC Adv.*, **2015**, 5, 98814-98821. The list of co-author includes Dr. Arash Akbari-Sharbat, Dr Reginald Bauld, Mr. Jaewoo Park, Dr. Michael Cottam, and Dr. Giovanni Fanchini. Tianhao Ouyang is the first author in this paper and is responsible for conducting the parametric study, performing scanning electron microscopy, atomic force microscopy, and scanning near-field optical microscopy presented in the paper and in this thesis. This work was conducted under the supervision of Dr. Giovanni Fanchini and Dr. Michael Cottam, they provided assistance for scientific analysis and editing of the paper.

Chapter 1 in this thesis is partially based on the introductory part of the paper. Mr. Jaewoo Park’s preliminary experiments suggested the possibility of this self-assembly and prompted the entire project discussed in this thesis.

Chapter 4 are partially based on the experimental results section of the paper. Dr. Reginald Bauld provided assistance during the use of scanning near-field microscopy system and contributed to the revision of the paper.

Results in Chapter 5 is partially based on the theoretical results section of the paper. Dr. Arash Akbari-Sharbat is responsible for carrying out the tight-binding model simulation.

Chapter 2 is an introduction to the experimental equipment used in the project and chapter 3 is the theory for our simulation methodology. These two chapters are based on literature review done by Tianhao Ouyang.

Acknowledgments

First, I would like to extend my gratitude to Dr. Giovanni Fanchini. As my supervisor, his passion for science, as well as the efforts he pays to educate students, have always been the beacon of guidance during my graduate career, pushing me for better achievement as a researcher.

Also, Dr. Michael Cottam has played an important role in the last two years of my study as my supervisor, his supervision is most considerate and encouraging. I thank him in the most heartfelt way for what I've learned from him as a scientist and a person.

I would also take this opportunity to thank Reginald Bauld and Sabastine Chukwuemeka Ezugwu, who are colleagues of mine for the last two years. Their help and guidance have led me out of the many difficult situations.

And my gratitude also goes to the rest of my group members, Arash Akbari-Sharbat, Jaewoo Park, Paul Bazylewski, Angela Ebere Ezugwu, Edith Pui Cheung Yeung, Ye Li, and Sina Kazemian.

I like to thank the department of physics and astronomy for all the support during the last two years.

Finally, I like to thank my families for supporting my decisions.

Table of Contents

Abstract.....	i
Co-Authorship Statement.....	ii
Acknowledgments.....	iii
Table of Contents.....	iv
List of Figures.....	vii
List of Abbreviations.....	xii
Chapter 1.....	1
1 Introduction to superlattices fabrication.....	1
1.1 Fabrication overview.....	3
1.2 Graphene thin films.....	3
1.2.1 Graphene fabrication methods.....	3
1.3 Deposition of the metallic layer.....	6
1.4 Nucleation of copper nanoparticles and self-assembly of superlattices.....	7
1.5 Optical properties of superlattices.....	8
1.6 Conclusion and thesis overview.....	9
1.7 Reference.....	10
Chapter 2.....	13
2 Fabrication and characterization: equipment and techniques.....	13
2.1 Fabrication equipment: nitrogen atmosphere glove box and vacuum deposition chamber.....	13
2.2 Characterization equipment.....	17
2.2.1 Scanning electron microscopy (SEM).....	17
2.2.2 Atomic force microscopy (AFM).....	19
2.2.3 Scanning near-field microscopy (SNOM).....	21

2.3	Near-field evanescent waveguide experiment using three-dimensional scanning near-field optical microscopy	23
2.4	Conclusion	26
2.5	References.....	27
Chapter 3.....		29
3	Theoretical methods.....	29
3.1	Properties of graphene	29
3.1.1	<i>Band structure of graphene and its defect</i>	29
3.1.2	<i>Graphene edge chirality</i>	31
3.2	Theoretical model of graphene	32
3.2.1	<i>Tight-binding model</i>	32
3.2.2	<i>Modified tight binding model for impurities</i>	35
3.3	Conclusion	37
3.4	Reference	37
Chapter 4.....		40
4	Parametric study in superlattices fabrication and its evanescent waveguiding properties.....	40
4.1	Parametric study of superlattices forming conditions.....	40
4.1.1	<i>Role of annealing temperature</i>	41
4.1.2	<i>Role of annealing time</i>	44
4.2	Secondary Cu-np features	47
4.2.1	<i>Parallel curving of Cu-np</i>	47
4.2.2	<i>Angles and preferable direction of alignment</i>	48
4.2.3	<i>Arrays of unevenly spaced lines of Cu-np</i>	49
4.3	Evanescent waveguiding properties.....	49
4.4	Conclusion	54

4.5	References.....	54
Chapter 5	56
5	Theoretical results and discussion.....	56
5.1	Copper atoms on graphene in uniform distribution and armchair arrays setting..	57
5.2	Copper atom lines on graphene at different chiral directions	59
5.3	Copper atoms lines on graphene at different interline distances	60
5.4	Conclusion	61
5.5	References.....	61
Chapter 6	62
6	Conclusion	62
6.1	References.....	63
Curriculum Vitae	64

List of Figures

Figure 1. 1: Diagram of fabrication procedure for superlattices of copper nanoparticles (Cu-np) of (i) deposition of a large area graphene thin film substrate (ii) thermal evaporation of a Cu layer on top of the film, and (iii) thermal annealing of the system with the formation of periodic arrays of Cu-np's superlattices.2

Figure 1. 2: Schematic of graphene thin film fabrication procedure, the solution-processed method uses a filter membrane to hold the graphene film and is later transferred to the substrate.4

Figure 1. 3: Scanning electron micrograph (SEM) showing the appearance of graphene thin film, despite overlapping with others, the produced graphene flakes are usually thin and formed by few-layer graphene.5

Figure 1.4: SEM image of graphene thin film covered with a Cu layer, it can be observed that, the deposition produced a homogenous and continuous layer on top of graphene flakes, this is vital for later procedure of obtaining a superlattice with the same Cu-np's size.6

Figure 1.5: (a) SEM image taken after thermal annealing of the graphene/Cu film under moderate condition, with the subsequent rearrangement of Cu into self-assembled superlattices of Cu-np's. (b) Region chosen from (a) to perform FFT, indicated by red rectangle. (c) Corresponding FFT pattern of (b), the bright line in the center region indicates a periodicity of the Cu-np lines in the same direction.8

Figure 1. 6: Schematic of confinement of near-field light scattering in Cu-np's superlattices, Cu-np lines provide a preferential direction for light propagation.9

Figure 2. 1: An overview picture of glove box used in our study. Deposition chamber (KJ Lesker) is attached to the left of the glove box, vacuum exchange chamber is attached to the right of the glove box.14

Figure 2. 2: Deposition chamber, (left): picture of the chamber, (right): schematic of the chamber, the deposition is carried out in vacuum environment, the source locates at the bottom of the chamber while the substrate locates at the upper region above the source. 15

Figure 2. 3: Schematic of the different types of electrons resulted from the interaction between the surface and the electron beam. It can be observed that, different types of signals come from different depth of the sample region.....18

Figure 2. 4: Schematic of (a) setup and working principle of AFM, (b) atomic interaction forces regime governing AFM measurement modes.20

Figure 2. 5: Schematic of types of SNOM operation modes based on how light is collected from the SNOM tip: (a) transmission-illumination, (b) transmission-collection, (c) illumination-collection, (d) reflection-illumination, (e) reflection-collection.22

Figure 2. 6: Diagram of the 3D-SNOM configuration used for measurements of topography and light scattering from Cu-np superlattices. Collection-mode and topography images are simultaneously obtained from an (X, Y) AFM/SNOM scan at $Z = 0$, while (X, Z) SNOM cross-section scans at selected regions enabled us to obtain the position of light scattered by the nanoparticles at different heights from the sample surface.....24

Figure 2. 7: Schematic of Mie scattering in different systems of Cu-np's: (a) coherent scattering in superlattices and (b) incoherent scattering combined with light absorption in randomly distributed Cu-np's.25

Figure 2. 8: Schematic of a Witec Alpha 300S system modified for 3D-SNOM imaging in reflection-collection mode, it can be observed that, in this mode, light illuminates the sample from the side.26

Figure 3. 1: Diagram of σ -bonds (in-plane) and π -bonds (out-of-plane) in graphene.....30

Figure 3. 2: Honeycomb lattice of Graphene at different directions: zigzag (red) armchair (green).31

Figure 3. 3: Hopping parameters in the presence of metal atoms on graphene, under the assumption that the six C atoms forming the central hexagon on the graphene lattice directly interact with the metal.35

Figure 3. 4: Simulations of single arrays of Cu along armchair (AC) and zigzag (ZZ) directions of a graphene lattice as well as for a uniform copper distribution with Cu:C = 1:8.36

Figure 4. 1: A diagram illustrating the different behavior of Cu-np's nucleated at different temperatures is also provided, showing a trend from semi-continuous and nano-structured Cu layers at the lowest temperatures to sparse assemblies at the highest temperatures, with superlattices forming at intermediate temperatures.41

Figure 4. 2: SEM images of samples annealed for 8 hours at low temperatures: (a) and (b) 200 °C, Cu layer remains in a semi-continuous state. (c) and (d) 280 °C, Cu-np lines feature has emerged, but superlattice with constant interline and interparticle spacing has not yet formed.42

Figure 4. 3: SEM images of samples annealed for 8 hours at ideal temperatures: (a) and (b) 360 °C, superlattice with constant interline and interparticle spacing is established.....42

Figure 4. 4: SEM images of samples annealed for 8 hrs. at high temperatures: (a) and (b) 440 °C, high temperature causes Cu-np to further nucleate, forming larger Cu-np's. (c) and (d) 480 °C, Cu-np disorderedly distributed has become the most common feature and lines feature is very rare.43

Figure 4. 5: Diagram illustrating the different behavior of Cu-np's self-assembly at different times, showing a trend from curved lines of Cu-np's at relatively constant distances Δy at the shortest times to isolated and coalescing lines of Cu-np's at the longest times, with superlattices forming at intermediate times.44

Figure 4. 6: SEM images of samples annealed at 360°C at short times (a) and (b) 1 hour, (c) and (d) 3 hours, and (e) and (f) 5 hours. It can be observed that, short annealing only prompts the Cu-np's to form into lines feature, but not superlattice.45

Figure 4. 7: SEM images of samples annealed at 360°C at ideal times (a) and (b) 8 hours, superlattice with constant interline and interparticle spacing is established. And long times (c) and (d) 12 hours, nucleation of Cu-np tends to happen faster at certain sites, resulting in the merging of lines at one ends.46

Figure 4. 8: SEM micrograph of curved lines of Cu-np's formed at 360°C for 5 hours, underlying graphene provides a topographical edge for the nucleation, resulting in curved Cu-np lines.47

Figure 4. 9: SEM image obtained from sample annealed at 500°C annealing showing Cu-np's lines along armchair edges of graphene domains.48

Figure 4. 10: SEM image obtained from sample annealed at 335°C and 8 hours showing Cu-np's lines with variable separation (a clear angular feature is also observable).49

Figure 4. 11: Typical AFM and (b) reflection-collection SNOM images obtained simultaneously from one of our Cu-np's superlattices annealed at 360°C for 8 hours. (c) SEM micrograph, obtained using FIB markers from the same sample region as in panels a and b. It can be observed that, AA' is between two Cu-np lines and BB' is along a region where Cu-np distributed disorderly.51

Figure 4. 12: Vertical SNOM scans in Z-direction for cross-sections indicated as A-A' (left) and B-B' (right) in Fig. 4. 11. The Z-axis extends from 0 to 1200 nm in this figure. It can be observed that, in AA' the light intensity decay gradually while in BB', additional peaks above the surface are present.52

Figure 4. 13: Scans in panel d show an exponential decay of the evanescent wave mode at a distance Z from the surface of section A-A' (corresponding to a periodic superlattice). Conversely, they show random interference patterns for section B-B' (corresponding to a random distribution of Cu-np's). The red line is a fit that demonstrates the exponential decay of the evanescent mode in section A-A'53

Figure 5. 1: Comparison of the density-of-states (DOS) for two different sets of distributions of Cu atoms on single-layer graphene: (a) uniform distribution and (b) arrays of Cu atoms along an armchair direction.....57

Figure 5. 2: (a) The DOS is calculated by using, in Eqn. 3. 14, the same ionization energy ($\epsilon_i = 0$) for all C atoms irrespectively of their contact or non-contact with Cu atoms. Hopping parameters $t_0 = t_1 = 2.90$ eV and $t_2 = 4.35$ eV were used. (b) The DOS is calculated by using different ionization energy ($\epsilon_i = 0$) for C atoms in contact with Cu ($\epsilon_i, Cu = +0.5$ eV). $t_0 = t_1 = 2.90$ eV and $t_2 = 4.35$ eV. It can be observed that, in both configuration, the armchair arrays distribution (blue) has the lowest DOS level.58

Figure 5. 3: Comparison of two different sets of arrays of Cu atoms: (a) along armchair vs. (b) along zigzag crystallographic directions of a graphene flake. (c) DOS of the armchair, zigzag and bare graphene configurations. It can be observed that, both armchair and zigzag distribution have a lower DOS level compared to bare graphene, and the armchair distribution has the lowestest DOS level among the three.....59

Figure 5. 4: (a) Theoretical formation energies of individual Cu-np's lines along armchair (AC) and zigzag (ZZ) directions and parallel lines of Cu-np's at an interline distance (y along AC directions. Minima for specific values of $\{y_i\}$ can be observed (with $y_1 = 1.0$ nm and $y_1 = 1.7$ nm evidenced in the plot). Each minimum corresponds to a favourable interline distance for the formation of superlattices. (b) Special case in the proximity of an armchair graphene edge, in which an irregular superlattice with multiple values of $\{y_i\}$ for parallel Cu-np's lines is shown.60

List of Abbreviations

a. u.	arbitrary unit
AFM	Atomic Force Microscopy
AC	Armchair
BSE	Back-Scattered Electrons
Cu-np	Copper nanoparticle
DC	Direct Current
DOS	Density of States
FFT	Fast Fourier Transform
FIB	Focused Ion Beam
HOMO	Highest Occupied Molecular Orbital
RNA	Ribonucleic acid
SE	Secondary Electrons
SEM	Scanning Electron Microscopy
SMA	Sub-Miniature Version A
SNOM	Scanning Near-Field Optical Microscopy

TB	Tight-Binding
TEM	Transverse Electromagnetic
ZZ	Zigzag
2D	Two-Dimensional
3D	Three-Dimensional

Chapter 1

1 Introduction to superlattices fabrication

Graphene is a structure consisting of bonded carbon atoms, in the form of a one-atom thick sheet. It has attracted a great deal of attention since the last decade. Research on the graphene-based material has led to many interesting results, such as using graphene as an alternative to transparent conducting indium tin oxide electrodes in organic solar cells, and using graphene in the lithium battery [1, 2]. Large area graphene films, however, are not yet widely commercialized. This is because the fabrication techniques needed to prepare high-quality graphene are expensive and non-scalable [3, 4]. Meanwhile, graphene-based thin films formed by assemblies of single-layer and multi-layer graphene platelets may offer unique means to translate engineered graphene-based materials from the realm of fundamental research, into practical applications in transparent and flexible electronics [5-7] in a more cost-effective way. Specifically, graphene thin films decorated with random distributions of metallic nanoparticles to enhance their optical and electronic properties have already been promising in specific applications [8, 9].

Attempts to decorate two-dimensional (2D) materials with metallic nanoparticles can be traced back over several years [10–12], expensive techniques normally suitable only over small areas are required to attain these nanopatterned structures on graphene or other 2D materials [13]. These “bottom-up” approaches include nanolithography and nano-contact printing. The spontaneous formation of superlattices of metallic nanoparticles on graphene-based materials on a generic substrate, nevertheless, has not yet been reported. Although disordered assemblies of size-selective Au particles on graphene were presented by Luo *et al.* [14], no periodic superlattices could be achieved.

In Ref. [15], Giovannetti *et al.* successfully demonstrated the shift in the band structure of graphene by applying metallic layers onto its surface. More specifically, this work showed that the effect has a great dependence on the specific type of metal used. When forming the chemical bond with the underlying graphene structure, it may significantly alter the band structure of graphene near the Dirac point in the case of some metals (such as Co, Ni, and Pd). Alternatively, another type of metals (Cu and Au), which only form weak bonding

with graphene, would cause shifts in the graphene Fermi energy without significantly changing its band structure. Later, in Ref [16], Akbari-Sharbaz *et al.* demonstrated the possibility to assemble metallic layers on top of graphene thin films both theoretically and experimentally with the metals that form weak bonding (such as gold [17] and copper [18]) with graphene to enhance some targeted aspects of graphene without dramatically changing the nature of the material. It is only recently, however, that calculations by Zhou *et al.* [19] suggested the possibility of self-assembling periodic arrays of alkali atom clusters along specific lattice direction of graphene. At a larger scale, attempts to decorate graphene-based material with metallic nanoparticles have been made, but the spontaneous formation of superlattices of metallic nanoparticles on graphene has never been experimentally produced, to the best of our knowledge.

In an attempt to decorate solution-processed graphene thin films with copper nanoparticles, the pattern of copper nanoparticles forming into a periodic structure on graphene was observed in our group. Such tendency suggested the possibility of the fabrication of the self-assembled metallic superlattices graphene, which prompted the study presented in this thesis. Understanding the mechanism of this self-assembly can help us achieve potential extensions to self-assembly of other materials, and new devices would emerge through self-assembling these nano-metallic phases into superlattices.

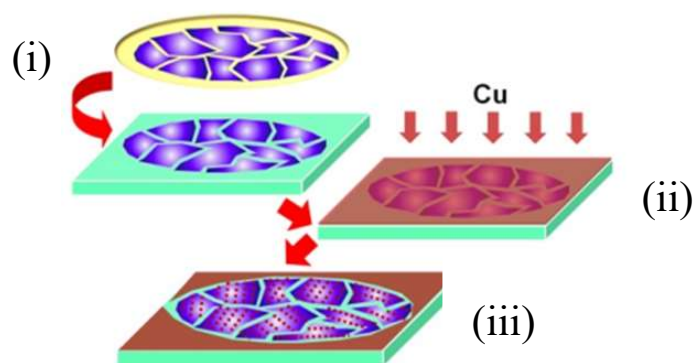


Figure 1. 1: Diagram of fabrication procedure for superlattices of copper nanoparticle (Cu-np) of (i) deposition of a large area graphene thin film on the substrate, (ii) thermal evaporation of a Cu layer on top of the film, and (iii) thermal annealing of the system with the formation of Cu-np superlattices.

1.1 Fabrication overview

In this chapter, we introduce the fabrication method of the self-assembled superlattices of copper nanoparticle (Cu-np). Conventionally, a superlattice is defined to be a periodic structure of layers of two or more material, in a 2D superlattice, it has an underlying layer with base (a, b) in the real space and lattice vector $r(m, n) = na + mb$, while the 2D superlattice itself has a superbase $(A, B) = (Na + Mb)$ and superlattice vector $R(m, n) = nA + Mb$, where n, m, N and M can be integer ranged from minus infinity to positive infinity. Thus our periodic structure of Cu-np lines with repeating interline and interparticle spacing is a 2D superlattice indeed. As shown in the diagram in Fig. 1. 1, the facile fabrication method consists of three main steps. Firstly, deposition of a large-area graphene thin film on a substrate, secondly, deposition of a thin Cu layer on top of the structure obtained in step one, and finally, applying thermal annealing to the structure obtained in step two for the formation of superlattices [20].

1.2 Graphene thin films

Graphene is a two-dimensional allotrope of carbon. Consisting of sp^2 hybridized carbon atoms, which are arranged in a honeycomb lattice, it forms a planar sheet of one atom thick. Due to its remarkable electronic and physical properties, graphene has attracted much attention in scientific and technological communities [21, 22]. As the fabrication techniques needed to prepare single-layer graphene are expensive and non-scalable, high-quality single-layer graphene is not yet widely commercialized [3, 4]. However, graphene thin films formed by single-layer and few-layer of graphene may offer unique means to translate engineered graphene-based materials from the realm of fundamental research into practical applications in a more cost-effective way.

1.2.1 Graphene fabrication methods

As discussed in detail in Ref. [23], graphene thin films produced by solution-processed methods are mainly formed by single-layer and few-layer graphene flakes. They were deposited by a method previously developed by Eda *et al.* [24] for graphene oxide laminates, and extended by Sharifi *et al.* [23] to obtain non-oxidized graphene thin films by using surfactant-assisted exfoliation of graphite. Ribonucleic acid (RNA) was used as a

nonionic surfactant, for exfoliation of graphite into single and few-layer graphene flakes in water solution and the subsequent preparation of transparent and conducting graphene-RNA thin films. A number of pre- and post-deposition treatments were performed to improve the electrical and optical performance of graphene-RNA thin films.

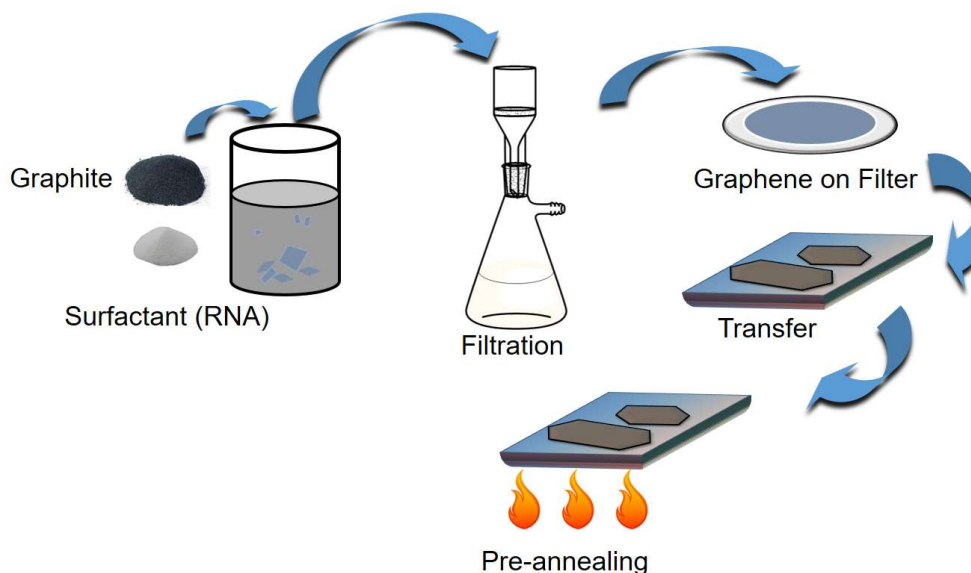


Figure 1. 2: Schematic of graphene thin film fabrication procedure, the solution-processed method uses a filter membrane to hold the graphene film and is later transferred to the substrate.

To fabricate graphene thin films, the first step is to exfoliate nanocrystalline graphite (Sigma-Aldrich, CAS 7782-42-5) in water using RNA. The RNA-graphite mixture solution is placed under sonication. As RNA contains both hydrophobic and hydrophilic groups while graphene is only hydrophobic, the surfactant can help breaking the bonding between two layers of graphene within the graphite during the process, producing large amounts of suspensions of single and few-layer graphene. The as-obtained aqueous dispersions of graphene are vacuum filtrated onto porous sacrificial membranes using a technique originally devised by Wu *et al.* [25] for carbon nanotubes. A volume of 3 ml RNA-based suspension with graphene is filtered through 0.4- μm pore diameter nitrocellulose membranes (Millipore, HTTP02500) to deposit the graphene flakes and to subsequently transfer the suspension onto the substrates. For our studies, these graphene-based thin films are deposited onto un-doped Silicon (100) substrates. Afterward, the filter membrane is left in contact with the substrate and dried at 80°C for 12 hours in a box oven. After drying, the

nitrocellulose filter membranes are etched with multiple acetone and methanol baths leaving behind a thin graphene-based film on silicon. Pre-annealing of the obtained substrate is conducted at 500°C for 3 hours to remove RNA from the surface of graphene. This is carried out in a nitrogen atmosphere to prevent oxidation from air. It also leads to the formation of some defects that were beneficial for metallic nanoparticles to adhere and nucleate if possible [26].

A typical scanning electron micrograph (SEM) of a bare graphene-based thin film we obtained is shown in Fig. 1. 3. The possibility to use solution-processed graphene thin films for our self-assembly experiments suggests that our superlattices fabrication method is highly tolerant to impurities and relatively insensitive to the number of graphene layers.

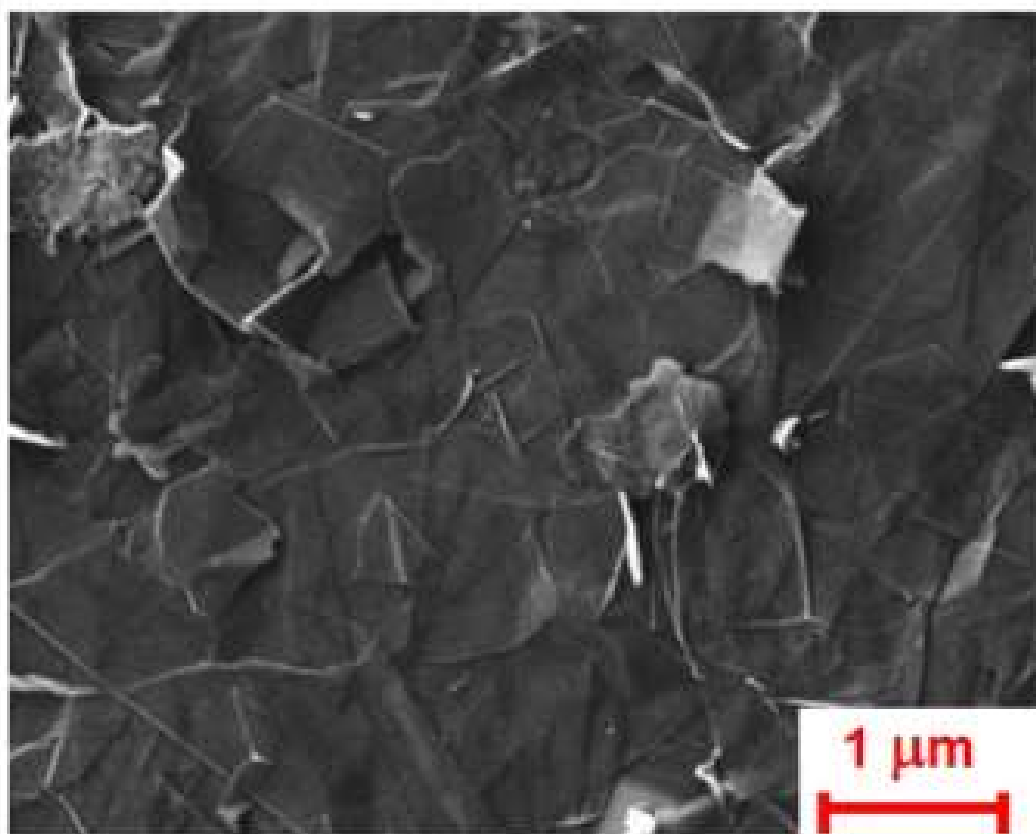


Figure 1. 3: Scanning electron micrograph (SEM) showing the appearance of graphene thin film, despite overlapping with others, the produced graphene flakes are usually thin and formed by few-layer graphene.

1.3 Deposition of the metallic layer

As the type and scale of the metallic layers could potentially determine the degree of enhancement of graphene, it is vital to gain an accurate control over the thickness during the deposition of the metallic layer. In our study, Cu was chosen to be the primary metallic source to be deposited onto graphene thin films. This is because, among the metals that form weak bonds to graphene, Cu is most commercially accessible. A thermal evaporation method is chosen to deposit Cu onto graphene-based thin films. In this method, a thermal evaporation system is used, which is installed in a high-vacuum chamber attached to a continuous glove box without any intermediate exposure to air.

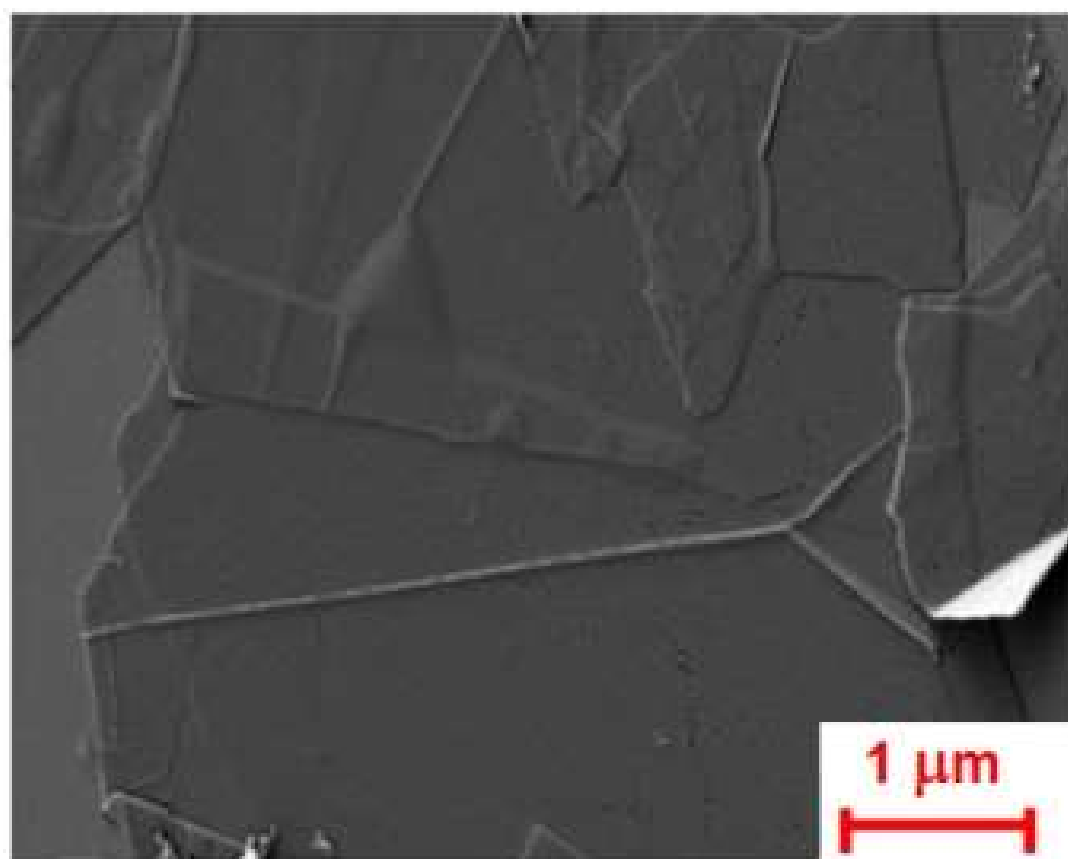


Figure 1.4: SEM image of graphene thin film covered with a Cu layer, it can be observed that, the deposition produced a homogenous and continuous layer on top of the graphene flakes, this is vital for later procedure of obtaining a superlattice with the same Cu-np's size.

During the evaporation process, Cu vaporizes at a high temperature and forms a cloud of metallic vapor, which is later deposited on the substrate and phases back to solid state. Details of the evaporation process are given in Chapter 2. The appearance of the obtained graphene-metallic thin films is shown in Fig. 1. 4.

1.4 Nucleation of copper nanoparticles and self-assembly of superlattices

The transformation of the metallic thin layer on the graphene thin films to Cu-np is crucial to the fabrication of superlattices. In our study, Cu-np's are formed on our graphene thin films by thermally-induced heterogeneous nucleation. This means that, within the flat Cu thin film, Cu clusters serve as sites for others to aggregate into. Such method, known as annealing, is an efficient thermal treatment to activate coalescence in the semi-connected metallic nanoparticles, forming individual metal islands as a result [27, 28]. Similar to the mechanism of dewetting [29], this is a process to achieve surface and interface energy minimization [30], depending on the annealing temperature, annealing time, film thickness, and substrate wettability of the metallic layer. Nevertheless, this thermal treatment would also prompt other oxygen-related reactions and lead to undesired oxidation if conducted in air. To prevent this, all samples are annealed inside the glove box in a nitrogen atmosphere with oxygen content no greater than 5 ppm.

In order to nucleate Cu-np's from the deposited Cu layers, the samples are extracted from the chamber and manipulated in the continuous glovebox. Once retrieved, samples are annealed in nitrogen atmosphere on a hot plate inside the glove box. A group of 25 simultaneously-grown samples is annealed under conditions that can be described by a 5x5 matrix: 5 groups of samples annealed at different temperature (200°C, 280°C, 360°C, 440°C, and 480°C), with each group annealed at 5 different times (1 hour, 3 hours, 5 hours, 8 hours and 12 hours). Other individual annealing under different conditions are also attempted. This study allows us to understand the role of temperature and time of the annealing, and what condition is more beneficial for the spontaneous formation of the superlattices. The fabrication produces 2D superlattices formed by periodic Cu-np lines, with a constant interline and interparticle spacing. A typical look of the superlattices is shown in Fig. 1. 5 (a). A region with obvious parallel-lines feature is chosen to obtain the

corresponding FFT pattern, indicated by panel b. A bright-line feature that locates diagonally at the center region can be observed in the FFT pattern in panel c, this suggests an interline periodicity of our superlattice along the same direction of the bright-line feature.

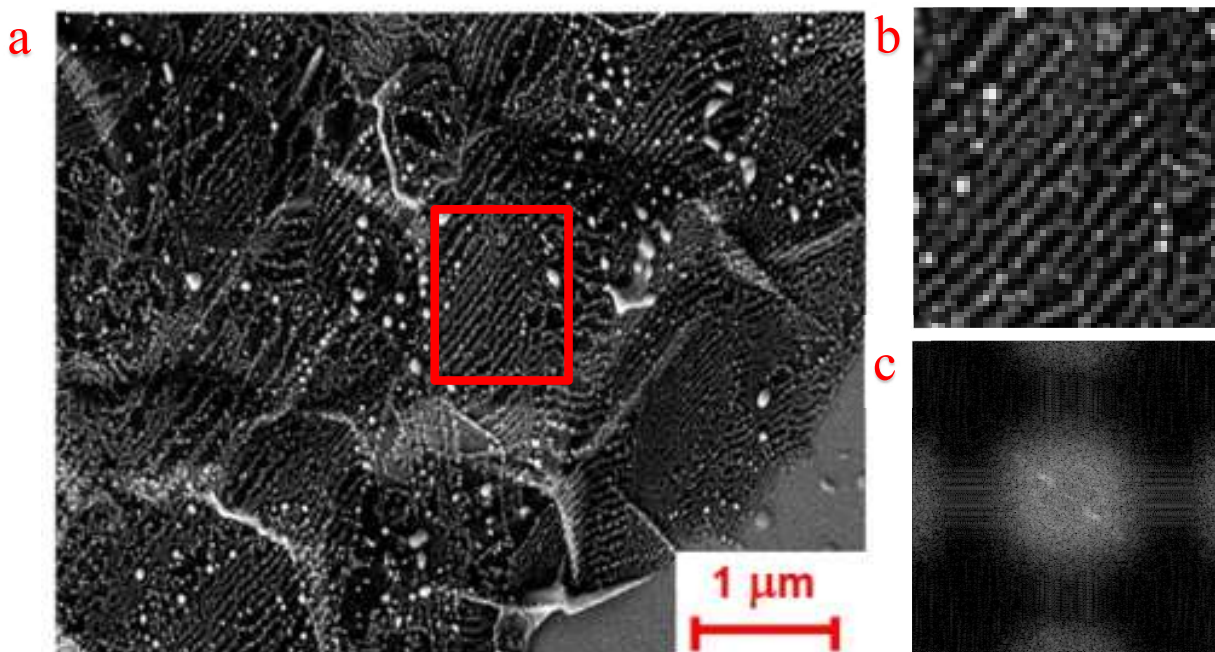


Figure 1.5: (a) SEM image taken after thermal annealing of the graphene/Cu film under moderate condition, with the subsequent rearrangement of Cu into self-assembled superlattices of Cu-np's. (b) Region chosen from (a) to perform FFT, indicated by red rectangle. (c) Corresponding FFT pattern of (b), the bright line in the center region indicates a periodicity of the Cu-np lines in the same direction.

1.5 Optical properties of superlattices

After the nucleation, the diameter of our self-assembled Cu-np's and their superlattice interparticle spacing is usually around 10–20 nm, while the superlattice interline spacing is roughly one order of magnitude larger. This makes the interline spacing of our superlattices comparable to the wavelength of visible light. As graphene offers an excellent platform for nanophotonics, an experiment is attempted to explore the evanescent waveguiding properties of our graphene-based Cu-np superlattices. This experiment explored the

superlattice's ability to channel near-field electromagnetic radiation. Described thoroughly in Chapter 2, the experiment uses a three-dimensional scanning near-field optical microscopy (3D-SNOM) technique previously developed by Ezugwu *et al.* [31]. This enables us to characterize our samples and extract the electric field intensity perpendicular to the air–superlattice interface. As shown in Fig. 1. 6, our superlattices can potentially provide multiple waveguiding tunnels as light travels along them. And later in Chapter 5, we will demonstrate the potential of our system to be used as a near-field waveguide in this thesis.

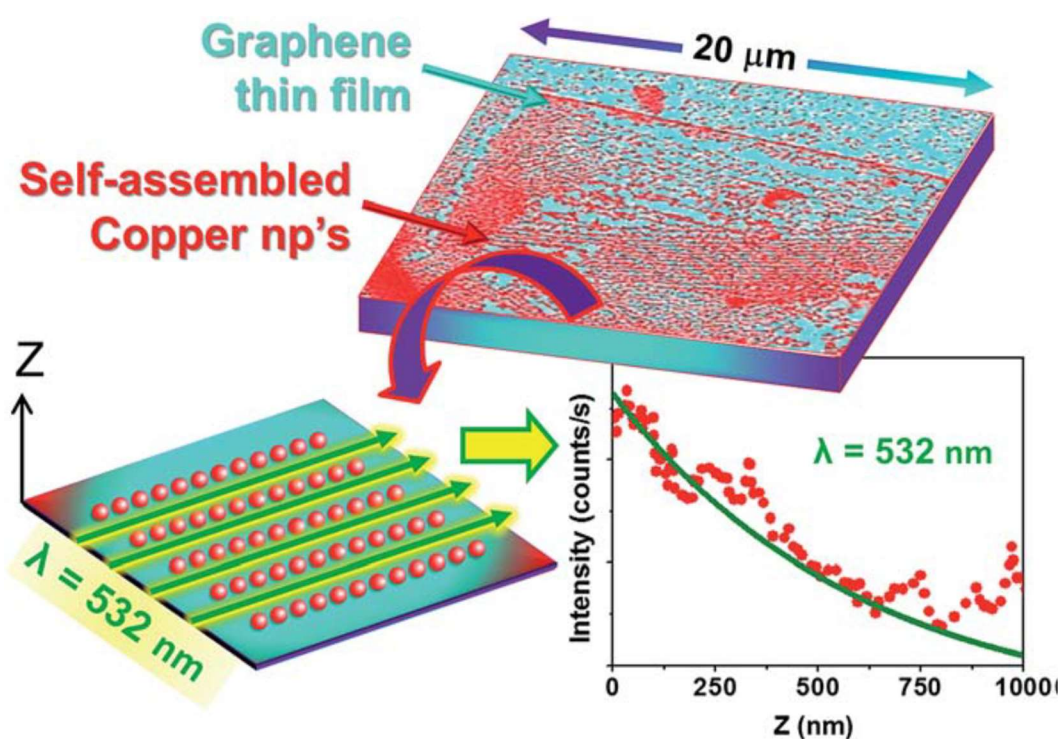


Figure 1. 6: Schematic of confinement of near-field light scattering in Cu-np's superlattices, Cu-np lines provide a preferential direction for light propagation.

1.6 Conclusion and thesis overview

Here in this thesis, we discuss the spontaneous assembly of superlattices of Cu nanoparticles (Cu-np) on single-layer to few-layer graphene thin films. This process is cost-effective, scalable and is suitable for potential extensions to nanoparticles of other metals that weakly bond to graphene [15] or to produce nanoparticle arrays on other 2D materials.

Yet, it is crucial to point out that the superlattices are obtained by a process consisting in the annealing at moderate temperatures of a thin copper layer that had not been previously exposed to air. This reminds us that the fabrication of these superlattices has to be carefully stimulated, and carried out in a suitable environment.

Therefore, in the next chapter, we will look into the equipment for the fabrication and their role in this study. Also, characterization techniques such as scanning electron microscopy (SEM) and scanning near-field optical microscopy (SNOM) will be discussed. As for Chapter 3, an introduction to the theoretical growth model is given. The experimental results of the superlattices fabrication under different annealing temperatures and times would be extensively discussed in Chapter 4. Also in this chapter, the attempt to preliminarily use the superlattices as a near-field evanescent waveguiding device is elaborated. In Chapter 5, through the theoretical simulations, a qualitative understanding of this spontaneous formation is achieved. By the end of this thesis, a summary of our work is given in Chapter 6.

1.7 Reference

- [1] S. Sun, L. Gao, and Y. Liu, *Applied physics letters*, **2010**, 96.8: 3113.
- [2] H. Kim, K.Y. Park, J. Hong, and K. Kang, *Scientific reports*, **2014**, 4, 5278.
- [3] R. Ruoff, *Nat. Nanotech.*, **2008**, 3, 10–11.
- [4] A. N. Obraztsov, *Nature nanotechnology*, **2009**, 4, 212.
- [5] R. Bauld, F. Sharifi, and G. Fanchini, *International Journal of Modern Physics B*, 2012, **26**, 1242004.
- [6] O. E. Andersson, B. L. V. Prasad, H. Sato, T. Enoki, Y. Hishiyama, Y. Kaburagi, M. Yoshikawa and S. Bandow, *Physical Review B*, 1998, **58**, 16387.
- [7] A. Milchev, E. Vassileva and V. Kertov, *Journal of Electroanalytical Chemistry and Interfacial Electrochemistry*, 1980, **107**, 323.

- [8] Y. Zhang, S. Liu, L. Wang, X. Qin, J. Tian, W. Lu, G. Chang and X. Sun, *Rsc Advances*, **2012**, 2, 538.
- [9] Y. Li, X. Fan, J. Qi, J. Ji, S. Wang, G. Zhang and F. Zhang, *Nano Research*, **2010**, 3, 429.
- [10] R. Muszynski, B. Seger and P. V. Kamat, *The Journal of Physical Chemistry C*, **2008**, 112, 5263.
- [11] S. Ghosh, I. Calizo, D. Teweldebrhan, E. P. Pokatilov, D. L. Nika, A. A Balandin, W. Bao, F. Miao, and C. N. Lau, *Applied Physics Letters*, **2008**, 92, 151911.
- [12] J. K. Lee, K. B. Smith, C. M. Hayner and H. H. Kung, *Chemical Communications*, **2010**, 46, 2025.
- [13] A. N. Shipway, E. Katz and I. Willner, *ChemPhysChem*, **2000**, 1, 18.
- [14] Z. Luo, L.A Somers, Y. Dan, T. Ly, N.J. Kybert, E.J. Mele and A.T.C. Johnson, *Nano letters*, **2010**, 10, 777.
- [15] G. Giovannetti, P. A. Khomyakov, G. Brocks, V. M. Karpan, J. Van den Brink and P. J. Kelly, *Physical Review Letters*, **2008**, 101, 026803.
- [16] A. Akbari-Sharbaf, M. G. Cottam and G. Fanchini, *Journal of Applied Physics*, **2013**, 114, 024309.
- [17] X. Yang, M. Xu, W. Qiu, X. Chen, M. Deng, J. Zhang, H. Iwai, E. Watanabe and H. Chen, *J. Mater. Chem.* **2011**, 21, 8096.
- [18] J. Luo, S. Jiang, H. Zhang, J. Jiang, X. Liu, *Analytica Chimica Acta*, **2012**, 709, 47.
- [19] J. Zhou, S. Zhang, Q. Wang, Y. Kawazoe and P. Jena, *Nanoscale* **2015**, 7, 2352.
- [20] T. Ouyang, A. Akbari-Sharbaf, J. Park, R. Bauld, M. G. Cottam and G. Fanchini, *RSC Adv.*, **2015**, 5, 98814-98821.

- [21] A. K. Geim, and K. S. Novoselov, *Nature materials*, **2007**, 6, 183.
- [22] A. K. Geim, *Science*, **2009**, 3, 1530.
- [23] F. Sharifi, R. Bauld, M. S. Ahmed and G. Fanchini, *Small*, **2012**, 8, 699.
- [24] G. Eda, G. Fanchini and M. Chhowalla, *Nature Nanotechnology* **2008**, 3, 270.
- [25] Z. Wu, Z. Chen, X. Du, J. M. Logan, J. Sippel, M. Nikolou, K. Kamaras J.R. Reynolds, D. B. Tanner, A. F. Hebard and A. G. Rinzler, *Science*, **2004**, 305, 1273.
- [26] A. Venter, M. Hesari, M. S. Ahmed, R. Bauld, M. S. Workentin and G. Fanchini, *Nanotechnology*, **2014**, 25, 135601.
- [27] O. A. Yeshchenko, I. M. Dmitruk, A. M. Dmytruk and A. A. Alexeenko, *Mat. Sci. & Eng. B*, 2007, 137, 247.
- [28] U. Pal, A. Bautista-Hernandez, L. R. Fernandez, J.C. Cheang-Wong, *J. of Non-Crystalline Solids*, **2000**, 275, 65.
- [29] S. Logothetidis, *Nanostructured Materials, and Their Applications*, Springer Science & Business Media, Heidelberg, **2012**.
- [30] G. Cao, *Nanostructures & Nanomaterials: Synthesis, Properties and Applications*, Imperial College Press, London, **2004**.
- [31] S. Ezugwu, H. Ye and G. Fanchini, *Nanoscale*, **2015**, 7, 252.

Chapter 2

2 Fabrication and characterization: equipment and techniques

In this chapter, the equipment used for the superlattice fabrication is thoroughly discussed. The containment of the graphene-Cu films within an inert nitrogen environment throughout the entire nucleation is imperative for the self-assembly to take place, since previous work of Luo *et al.* [1], which was done in a comparable fashion with the exception that the graphene-metal layer was exposed to air before thermal treatment, has demonstrated disordered assemblies of size-selective Au particles on graphene with no periodic structures observed. Therefore, it should be emphasized that the continuous setup of the glove box and vacuum deposition chamber acts as an important role in the spontaneous formation Cu-np superlattice.

Also, characterization techniques such as scanning electron microscopy (SEM), atomic force microscopy (AFM) and scanning near-field optical microscopy (SNOM) are briefly introduced, while the experimental setup for testing the near-field evanescent waveguiding properties based on a novel technique developed by Ezugwu *et al* [2] is elaborated.

2.1 Fabrication equipment: nitrogen atmosphere glove box and vacuum deposition chamber

One of the major advantages of our facility is the integration of the glove box and deposition chamber developed by Ezugwu *et al* and extensively discussed in Ref. [3]. The glove box (Nexus II, Vacuum Atmospheres Inc.), an enclosure filled with nitrogen gas, is designed specifically for experiments that couldn't be conducted in an oxygen environment, as well as temporal storage of samples that are sensitive to oxygen, since the nitrogen atmosphere limits undesirable oxidation.

A picture of the continuous setup is shown in Fig. 2. 1. At the right side of the glove box, a chamber is added, which can be opened from both the inside of the glove box, as well as from the outside environment. Connected to a rough vacuum pump, this chamber is responsible for the material exchange between the outside environment and the glove box.

Despite the fact that the exchange chamber is usually kept in vacuum state, it is capable of operating in air and nitrogen. When the chamber needs to be opened, the nitrogen from the glove box is released to enter the chamber, allowing the chamber to adjust the level of pressure, so it can be opened from both the inside of the glove box and the outside environment. Importantly, once the chamber is exposed to the outside environment, ‘purging procedure’ must be carried out, before allowing a direct connection to the glove box. This procedure consists of multiple evacuations of gas and refilling it with nitrogen. Such precautions can prove vital to maintaining a low level of oxygen and moisture within the glove box. And based on the same reason, to further reduce the accumulation of oxygen and moisture, the purging procedure is also carried out for the glove box in a routine schedule.

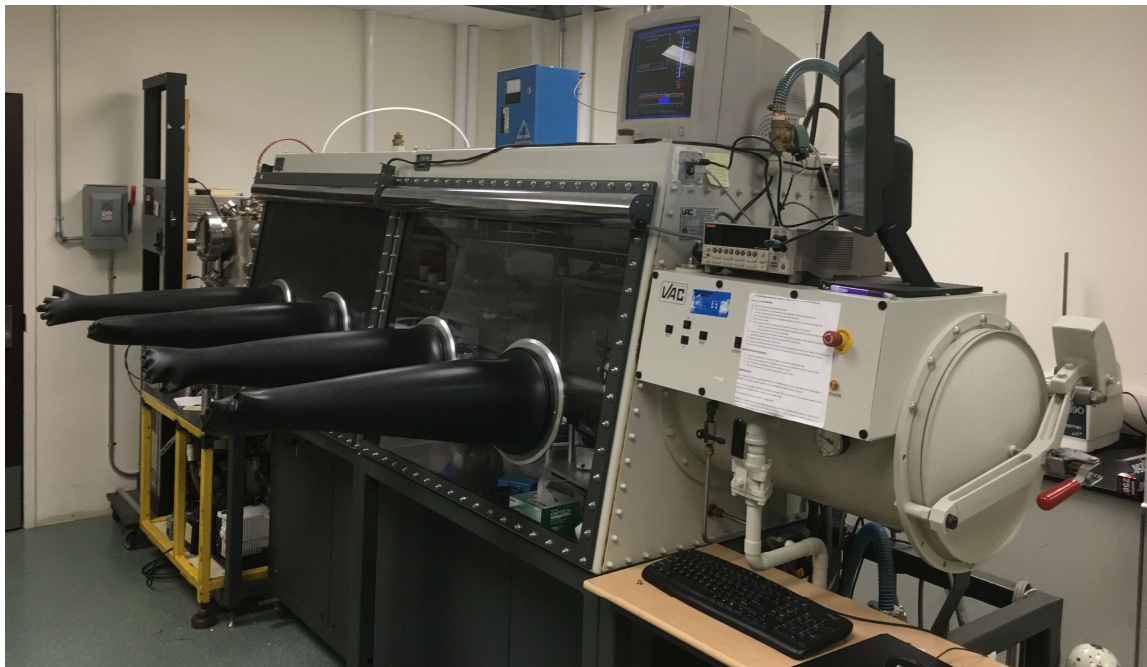


Figure 2. 1: An overview picture of glove box used in our study. Deposition chamber (KJ Lesker) is attached to the left of the glove box, vacuum exchange chamber is attached to the right of the glove box.

The deposition chamber (KJ Lesker) is attached continuously to the left of the glove box. This conveniently allows samples to be processed without intermediate exposure to air between the deposition and later manipulation, specifically, the annealing process performed inside the glove box using hotplate (Cole-Parmer StableTemp ceramic hot plate).

In our study, thermal evaporation, a popular technique for thin-film deposition, was used to obtain Cu thin film. As indicated in the diagram in Fig. 2. 2, thermal evaporation is performed at a vacuum state, with the source and the substrate placed inside the chamber, where the source is thin film material and the substrate is the targeted platform for the deposition. Despite usually kept in vacuum state, the vacuum chamber can be accessed from the glove box when the pressure of the two are at the same level. This can be achieved by channeling fresh nitrogen into the chamber. Two phase transitions are accountable for this technique: sublimation of the source from solid state to gaseous state, and the deposition of these gasses back to the solid state [4].

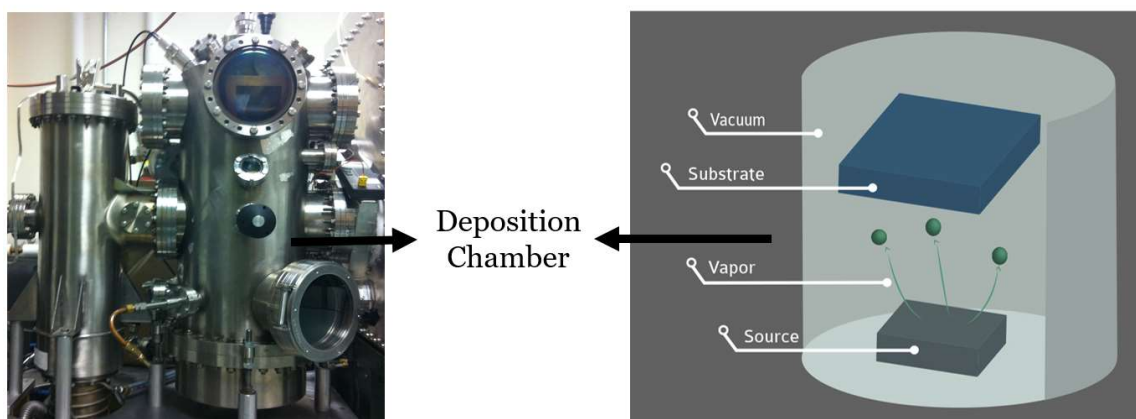


Figure 2. 2: Deposition chamber, (left): picture of the chamber, (right): schematic of the chamber, the deposition is carried out in vacuum environment, the source locates at the bottom of the chamber while the substrate locates at the upper region above the source.

A high vacuum state in the deposition chamber is necessary for the evaporation. A pressure level lower than 10^{-9} mmHg, the impurities inside the chamber other than the source material are largely removed, offering an environment for evaporated vapor to achieve a stable flow rate, and hence the deposited layer on the substrate is pure and uniform. In our case, a pressure level at 10^{-10} mmHg was achieved in our case. In low vacuum however, on the one hand, the impurities in the ambient if not eliminated can potentially react with the source vapor, inducing unwanted ingredient in the thin film. This guarantees the deposited layer on the substrate is pure and uniform, on the other hand, the unwanted

reactions reduce the amount of vapor that reaches the substrate, making the thickness difficult to control [5].

In our study, a Cu wire with a 99.999% purity is chosen to be the source, placed in an alumina crucible surrounded by a tungsten filament heater. As the filament is heated up, Cu wire melted and formed a pool in the crucible and evaporated into a cloud above the source and deposited onto a turnable square substrate holder that is approximately 50-cm above the source. Subsequently, the vapor particles returned back to a solid state after it made contact with the substrate, in our case, silicon (100) wafers, producing a Cu layer of certain thickness. A desired thickness of the deposited layer can be obtained accurately by controlling the flow rate of the vapor. The system uses a Sycom STM-2 quartz-oscillator to monitor and an RF VII Inc. RF3 generator and PT-II-CE matching network to control the process. The generator provides current and voltage to the tungsten filament to heat up the crucible. As a hotter source generates more vapor, controlling the current and voltage at a suitable level to obtain a small and steady flow rate is essential for the accuracy of the thickness. The key concept behind the monitoring is that the quartz-oscillator is mounted inside the vacuum chamber to receive deposition in real time and be affected by the deposition in a measurable way. This is achieved through the use of quartz crystal. Specifically, the oscillation frequency will drop as the crystal's mass is increased by the material being deposited on it, and it is being continuously read and calculated to convert the frequency data to thickness data, producing both instantaneous rate and cumulated thickness. In this thesis, a thickness of 0.7 ± 0.3 nm was used throughout the entire study, with a current of 70 A and voltage of 8.5 V from the generator, 0.05 nanometer/second for deposition rate and 10 seconds for the deposition time.

Noticeably in our case, as the silicon substrate is smooth, the roughness of the deposition relies entirely on the quality of the graphene thin film. Our graphene thin films produced by the solution-processed process are reported to be flat and usually within few hundred nanometers in thickness. Hence, the phenomenon of shadowing [6], which results in a non-uniform deposition due to a rough surface with protruding features blocking the evaporated material from some areas, can be treated as a minor effect and thus neglected.

2.2 Characterization equipment

Both scanning electron microscopy (SEM) and atomic force microscopy (AFM) are capable of providing nanometer-scale information about a material, but SEM was chosen to be the primary imaging tool. This is because AFM relies on the force interaction between the probe and the sample, an image at high resolution usually requires a long scanning time, compared to the resolving time of SEM. Furthermore, SEM provides a large depth of field that allows imaging at different magnification of the sample at different locations, whereas AFM can only highly resolve a relatively small area due to the limitation imposed by the short probe-sample interaction distance.

In our study, AFM and scanning near-field microscopy (SNOM) are performed simultaneously [7, 8]. SNOM is a technique to measure optical properties using the property of evanescent wave. An evanescent field, or evanescent wave, is an oscillating electric and/or magnetic field which does not propagate as an electromagnetic wave but whose energy is spatially concentrated in the vicinity of the source. Thus, the evanescent wave stores the spatial information near its surface within one wavelength distance. This helps SNOM to achieve subwavelength resolution based on the interaction of two objects, a nanoparticle and the aperture of the tip, or a nanoparticle and an apertureless tip. In the experiment of testing the waveguiding properties of our superlattices, AFM and SNOM were carried out for investigating the optical properties of the superlattices.

2.2.1 Scanning electron microscopy (SEM)

SEM uses an electron gun to produce electron beam, a narrow electron beam creates a large depth of field. The electron beam is first emitted to interact with the sample, the surface information of the sample is produced by the interaction between the electron beam and atoms at various depths within the sample. Then, the corresponding signals that contain surface information are collected to produce an image, yielding a characteristic two-dimensional surface structure of a sample. During our analysis, the SEM images we obtained are 2D intensity maps in the digital domain. Each image pixel on the display corresponds to a point on the sample, which is proportional to the signal intensity captured by the detector at each specific point. Since the images are formed by electrons emission,

no optical transformation takes place nor real optical images are produced. The magnifications of SEM usually range from 10 times to more than 500,000 times, which is about 250 times higher than the magnification limit of the best light microscopes. With the help of the field emission gun especially, images produced can usually resolve objects that are smaller than 10 nanometers. And to achieve higher magnification, a longer scan on the sample is required, as magnification is given by the ratio between the duration of the scan on the sample and a constant duration of a scan on the monitor [9].

In our study, all samples were characterized using a field emission SEM that operates in a vacuum environment at 1kV (Zeiss LEO 1540XB) [10]. At this setting, several types of signals are produced, which includes secondary electrons (SE), back-scattered electrons, and photons of characteristic X-rays. The standard operation mode of SEM is based on collecting the signal of the SE, and hence it is called secondary electron imaging, which is employed in our study as the main SEM imaging method. Secondary electrons are ionization products, generated by other radiation, in the form of ions, electrons, or photons with sufficiently high energy. In this specific case, secondary electrons are ejected from the k-shell by the inelastic scattering interactions with beam electrons, emitted from an area very close to the sample surface (few nanometers). Consequently, SEM can produce very high-resolution images of a sample surface, revealing details in a nanoscale [11].

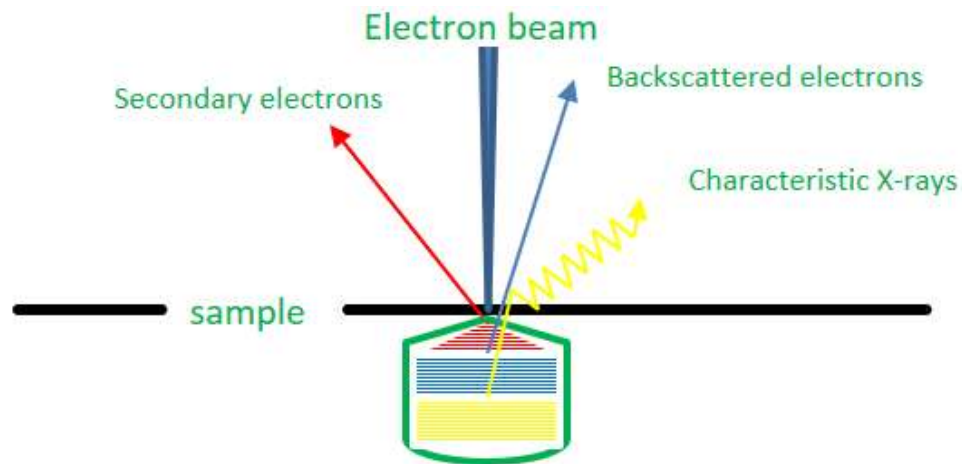


Figure 2. 3: Schematic of the different types of electrons resulted from the interaction between the surface and the electron beam. It can be observed that, different types of signals come from different depth of the sample region.

BSE are electrons elastically reflected backwards from deeper regions all over the of the sample, this is indicated in Fig. 2. 3 [12]. Consequently, these electrons can only be directed in BSE mode, and the resolution of BSE images is generally poorer than SE images. Nonetheless, BSE is more frequently used for compositional analysis, as the intensity of the BSE signal is strongly related to the atomic number (Z) of the material of the sample. This technique utilizes the signal produced by photons of the characteristic X-rays as well. When inner shell electrons are ejected from the sample, electrons with higher energy in the outer shell releases some of its energy to fill the vacant position in the shell. During this process, characteristic X-rays in a pattern that is characteristic of the type of the element is emitted. Therefore, the compositional analysis uses BSE images to provide information about the distribution of different elements in the sample while the characteristic X-rays are used to identify the elements and measure its abundance in the sample [12].

Other than imaging and compositional analysis, SEM can also be combined with sputtering and milling by focused ion beam (FIB) [13]. FIB operates in a similar fashion to SEM imaging. Rather than using a beam of electrons, FIB uses a finely focused beam of ions (usually gallium) that can be operated at high beam currents for site-specific operation at a nano-scale. The beam provides a high level of surface interaction when operated at high current. Through this, material on the sample surface can be removed by sputtering, allowing precision milling at a micrometer level. Using this method, a 1 mm long marker was applied in the proximity of a region near one of our superlattices. This is intended for the evanescent waveguiding experiment, where AFM and SNOM measurements need to be performed at the same region.

2.2.2 Atomic force microscopy (AFM)

Aside from SEM, the surface analysis and morphological mapping for the superlattices were also studied using a Witec Alpha 300S atomic force microscope. A typical AFM setup is shown in panel a, Fig. 2. 4. The system is interfaced with a desktop computer for controlling different parts and data collection. Besides AFM, the system is also capable of performing imaging techniques such as confocal microscopy and SNOM. As these measurements are very sensitive to mechanical vibrations, electromagnetic waves, and acoustic noise, our AFM system is contained within an anti-damping enclosure. In our

work, SNOM measurements were carried out for the investigation of the waveguiding properties of superlattices, during which AFM images were also produced simultaneously with the SNOM images.

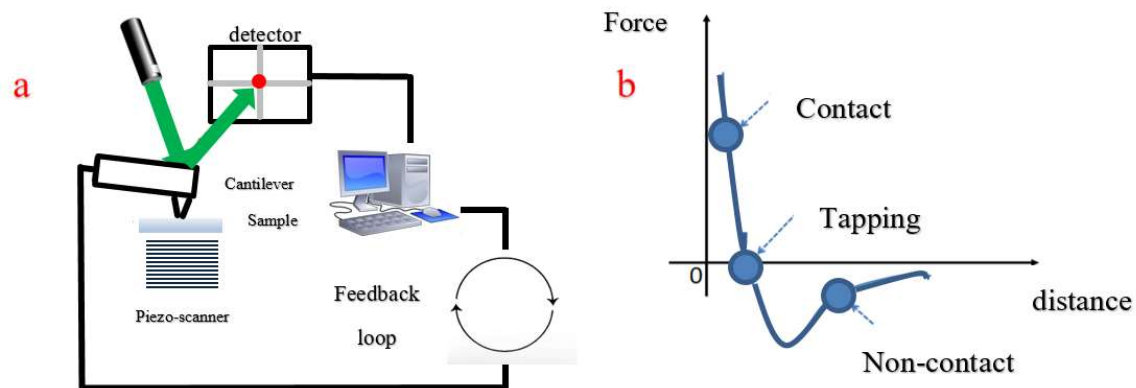


Figure 2. 4: Schematic of (a) setup and working principle of AFM, (b) atomic interaction forces regime governing AFM measurement modes.

As shown in panel a, to image the morphology of the superlattices, the sample is placed on a piezoelectric scanner that can move precisely in different directions in response to the applied voltage, and probed by a tip attached to the free end of a cantilever. The force the sample and the tip establishes on each other results in deflecting the cantilever, the detector picks up the deflection signal which is later processed by a computer to create the surface morphology of the sample.

In Fig. 2. 4, panel b, the force associated with the cantilever deflection is an interatomic force which contains two components: short range repulsive forces and long-range attractive forces, depending on the separation between the tip and sample. When the separation distance is long enough, the van der Waals force between the ions of the tip and electrons of the sample or vice versa becomes dominant, producing an attractive force. On the contrary, when the tip and the sample are brought into very close proximity with each other, the electrostatic repulsion between the electron clouds of them becomes dominant, producing a repulsive force. Hence, depending on the separation, three operating modes for AFM have been established including contact, non-contact, and intermittent contact modes as elaborated in Ref. [14].

In our work, contact mode was the primary mode used. In this mode, the tip is brought into proximity of the sample of only a few angstroms, creating soft physical contact with the sample surface. At this distance, the repulsive force is dominant because electronic clouds of the tip and the sample's atoms strongly repel each other. The type and magnitude of the force exerted by the cantilever on the tip depend on the deflection of the cantilever, which is proportional to the height of the scanning region of the sample surface. Typically, the deflection of the cantilever is detected by measuring the displacement of a laser beam reflected from the back side of the cantilever using a position sensitive photodetector. As the cantilever deflects, the deflection is sensed and compared in a DC amplifier in the feedback loop to some desired value of deflection. When the measured deflection is different from this value, the feedback loop will apply a voltage to the piezo-scanner. This will change the vertical position of the sample relative to the cantilever, restoring the desired value of deflection. The voltage that the feedback loop applies is a measure of the height of features on the sample surface, which is displayed as a function of the lateral position of the sample, allowing for the imaging of the morphology of the sample in three dimensions.

2.2.3 Scanning near-field microscopy (SNOM)

Scanning near-field optical microscopy (SNOM) is an imaging technique that circumvents the intrinsic diffraction limit of the conventional optical microscope, allowing us to investigate the optical properties at a small scale, which is suitable for the study of our superlattices at a scale of few nanometers at minimum [8]. In SNOM, the subwavelength resolution is achieved by utilizing the property of evanescent waves, generated in the proximity of an object, which is near-field in nature. As these evanescent waves do not propagate as electromagnetic waves, the energy of them are spatially concentrated in the vicinity of the source and decay exponentially as the distance increases from the source.

In our study, SNOM images were recorded using an aperture-type SNOM system, which uses a scanning probe with an aperture at the tip. The tip size is typically on the order of 100 nanometers, which allows light to pass through but also contains it within a very small area. The integration of AFM and SNOM technique is an advantage of modern near-field

microscopes. Through the use of an aperture-type SNOM tip, AFM and SNOM images can be recorded simultaneously. As the tip-sample force interactions create AFM images, SNOM images are created due to light interactions between the tip and the sample. Once illuminated, the movement of the sample controlled by piezo-scanner generates different evanescent light profiles due to different regions on the sample, and these profile is collected using photo-detector, which outputs a value for a given intensity and assigns that value to a corresponding pixel in the SNOM image [4].

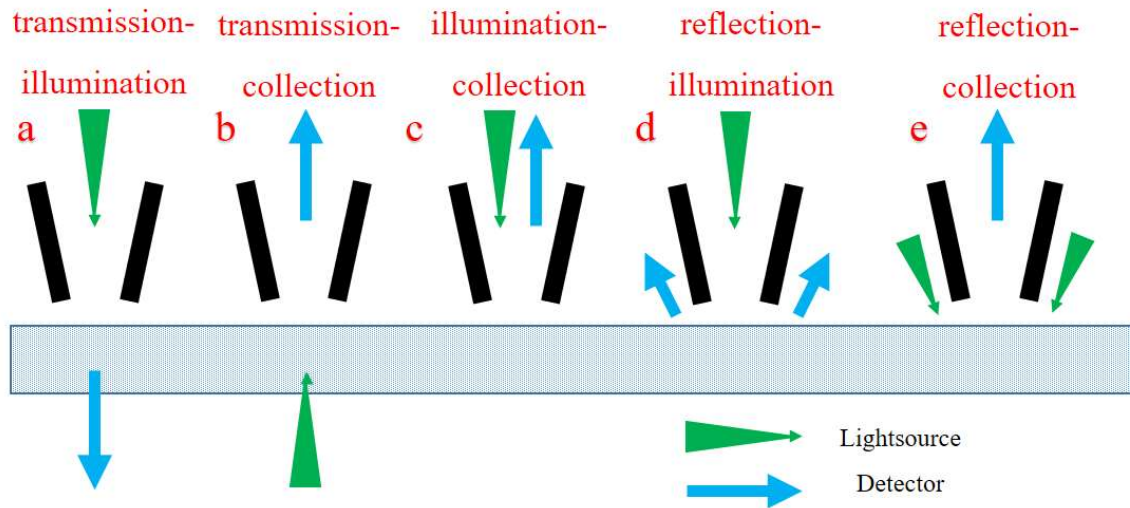


Figure 2. 5: Schematic of types of SNOM operation modes based on how light is collected from the SNOM tip: (a) transmission-illumination, (b) transmission-collection, (c) illumination-collection, (d) reflection-illumination, (e) reflection-collection.

Typically, there are five different operation modes in SNOM, as shown in Fig. 2. 5. The main difference between these modes is how the evanescent field is collected [3]. In transmission-illumination mode, the light comes from the top and goes through the SNOM tip to the detector. In transmission-collection mode, the light comes from beneath and goes through the SNOM tip to the detector. In illumination-collection, the light comes from the top and goes through and reflects vertically back to the SNOM tip and to the detector. In reflection-illumination, the light comes from the top and goes through and reflects horizontally around the SNOM tip to the detector. And in reflection-collection, the light illuminate the sample horizontally around the SNOM tip and reflects vertically through the tip to the detector. Generally, transparent samples are required for any transmission mode.

In our case, the superlattices are located on a silicon wafer, a non-transparent substrate, therefore, modes other than transmission seem to provide more flexibility for further investigations.

2.3 Near-field evanescent waveguide experiment using three-dimensional scanning near-field optical microscopy

Investigation of the waveguiding properties of our superlattices was conducted using a three-dimensional SNOM technique developed by Ezugwu *et al.* [2]. As the illumination source, in our case the Cu-np, it emits evanescent waves in its proximity in any direction, SNOM images in (X, Y) plane at $Z = 0$ are produced using these near-field features, when the collection takes place sufficiently close to the source, usually at the order of the wavelength of the incident light. However, as the tip moves away from the source, a response corresponding to the far-field features are observable. 3D-SNOM was designed specifically for this reason. In addition to the near-field features we observed from the images produced by the conventional SNOM, an extra image produced at a nonzero Z is taken to reveal the light profile at a far distance from sample surface.

With this technique, the ability of our superlattices to sustain the propagation of evanescent waves confined in the proximity of the graphene surface, and along the direction parallel to the lines of Cu-np can be probed. 3D-SNOM experiments were carried out in reflection-collection mode as demonstrated in Fig. 2. 6. This 3D optical imaging procedure is capable of reconstructing the electromagnetic field around the superlattices entirely, since positioning the piezo-scanner at different heights can produce SNOM images at different Z . In these experiments, the superlattice is positioned at a direction that the Cu-np lines are parallel to the X-axis. Then, the light source is launched into an optical fiber and positioned to illuminate at a direction parallel to the sample surface and the Cu-np lines, at a height which corresponds to the tiny gap between the surface and the aperture-type atomic force microscopy (AFM)-SNOM tip. Thus, modes generated by the laser source, which is evanescent in Z -direction and propagating along the sample surface, can be locally

collected at any (X, Y, Z) location by the AFM-SNOM tip aperture and then guided to the confocal microscope focused upright.

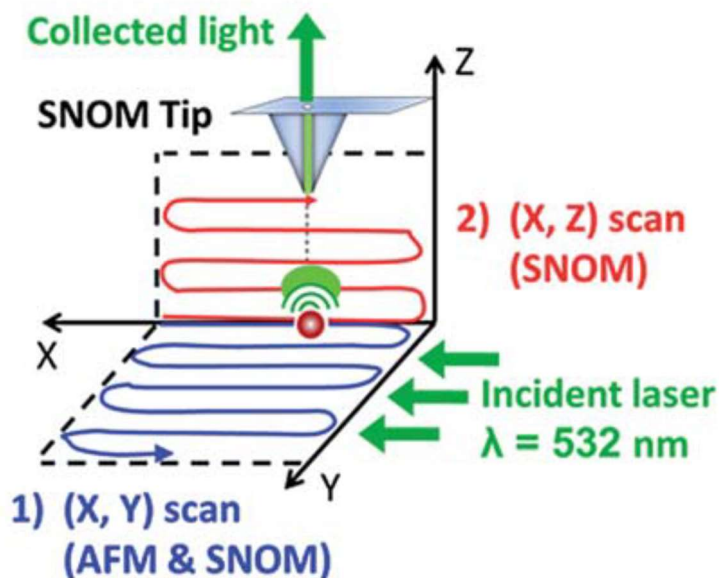


Figure 2. 6: Diagram of the 3D-SNOM configuration used for measurements of topography and light scattering from Cu-np superlattices. Collection-mode and topography images are simultaneously obtained from an (X, Y) AFM/SNOM scan at $Z = 0$, while (X, Z) SNOM cross-section scans at selected regions enabled us to obtain the position of light scattered by the nanoparticles at different heights from the sample surface.

Specifically, during each 3D-SNOM measurement, a contact-mode AFM-SNOM scan is first performed and the distribution of the intensity of near-field within the (X, Y) plane is probed in the close proximity of the surface, as shown in Fig. 2. 6, step (1). This measurement provides an AFM scan of the sample surface in conjunction with the (X, Y) SNOM scan at $Z = 0$. Reproducible tip position relative to the sample is obtained with an (X, Y) piezo-scanner and a controlling feedback loop. In a second measurement step (step 2 in Fig. 2. 6), an (X, Z) SNOM scan is carried out at increasing Z by selecting a specific cross section X , obtained from the (X, Y) image. In order to perform this operation, the distance Z between the tip and the sample surface is increased, operating in the (X, Z) plane, with $Z = 0$ to be set at the point at which the tip is in contact with the sample. As

mentioned above, this procedure enables us to study the scattered waves and their propagation at different vertical positions. And thus, it is repeated at decreasing tip-sample distance until contact with the surface is restored.

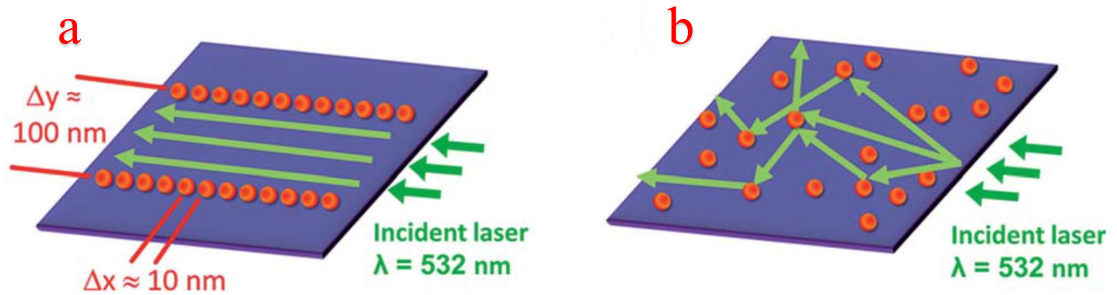


Figure 2. 7: Schematic of Mie scattering in different systems of Cu-np's: (a) coherent scattering in superlattices and (b) incoherent scattering combined with light absorption in randomly distributed Cu-np's.

SNOM (X, Z) scans were specifically used in our study for probing the decay of near-field evanescent modes away from the sample surface. Vertically, evanescent fields only exist within about one wavelength of incident light. In the near field, scattering dominates the interaction between light and our superlattices, as Cu-np's are known to display strong Mie scattering at $\lambda = 532$ nm [15, 16]. Parallel Cu-np's lines with interline distances ($\Delta y \sim 10^2$ nm) of the same order of magnitude as the incident wavelength provide a preferential direction for Mie scattering [16]. Light is only absorbed transversally to Cu-np's lines, leaving only scattering with little attenuation for longitudinal modes, hence an evanescent wave can be confined (Fig. 2. 7a). Conversely, the light will be isotropically scattered in all directions by randomly distributed Cu-np's (Fig. 2. 7b) causing interference between far-field modes along Z .

The setup of reflection-collection mode SNOM measurements is indicated in Fig 2. 8. A 50-mW power, 532 nm solid state laser (Excelsior, Spectra Physics Inc.) was connected using an SMA beam collimator attached to the fiber ending to illuminate the sample. The location and orientation of these Cu-np's lines were indicated by a micron-level marker previously produced by FIB, in this way, fine adjustment of the position of the sample and

the laser to align the Cu-np's lines and the laser beams were possible using a high-resolution confocal microscope. This procedure is for allowing a sufficient amount of light for scattering and to maximize the waveguiding effect. When scanning, the light scattered at the sample surface was collected from the 80 nm diameter aperture of a hollow AFM-SNOM tip (SNOM-C, NT-MDT Co. Moscow, Russia) mounted on the confocal microscope. The collected light was subsequently channeled into another SMA optical fiber connected to a photomultiplier tube (U-68000, Hamamatsu) operating in photon-counting mode. In our 3D-SNOM, the (X, Y) scan was conducted on the surface plane at $Z = 0$. Subsequently, the (X, Z) SNOM scan was conducted by selecting a specific cross-section parallel to the propagating direction of the incident laser in the obtained (X, Y) scan to obtain relevant information about the amount of light scattered by the particles at different heights above the sample surface, therefore, without changing the direction of the illumination by the laser, (X, Z) SNOM scans of two different configurations, parallel Cu-np's lines and randomly distributed Cu-np's, produced a comparison of light scattering of two different Cu-np's orientations. These results will be presented in Chapter 4.

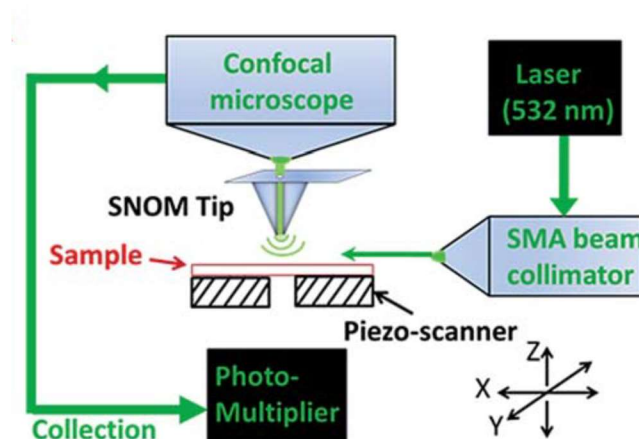


Figure 2. 8: Schematic of a Witec Alpha 300S system modified for 3D-SNOM imaging in reflection-collection mode, it can be observed that, in this mode, light illuminates the sample from the side.

2.4 Conclusion

In this chapter, the general introduction to the characterization techniques is given, including SEM, AFM and SNOM. The 3D-SNOM technique was emphasized along with

the reflection-collection Witec Alpha setup for the waveguiding experiments carried out for investigation of the optical properties of our superlattices. Results of the parametric study and the waveguiding experiment will be presented and discussed in Chapter 4. Equally, in Chapter 3, we will discuss the theoretical model which we used to investigate the formation of the superlattices.

2.5 References

- [1] Z. Luo, L.A Somers, Y. Dan, T. Ly, N.J. Kybert, E.J. Mele and A.T.C. Johnson, *Nano letters*, **2010**, 10, 777.
- [2] S. Ezugwu, H. Ye and G. Fanchini, *Nanoscale*, **2015**, 7, 252.
- [3] S. Ezugwu, *Synthesis and characterization of copper nanoparticles and copper-polymer nanocomposites for plasmonic photovoltaic applications*. MSc thesis. The University of Western Ontario, **2012**.
- [4] G. W. Neudeck, and F. P. Robert. *Modular Series on Solid State Devices*, **2002**, 5.
- [5] D. Smith, *Thin-film deposition: principles and practice*. McGraw Hill Professional, **1995**.
- [6] T. H. V. Thi, P. Brault, J. L. Rouet, and S. Cordier, *arXiv preprint math-ph/0609012*, **2006**.
- [7] <http://www.witec.de/>
- [8] M. De Serio, R. Zenobi, V. Deckert, *Trends in Analytical Chemistry*. 22(2), 70 - 77 (2003).
- [9] G. Lawes, *Scanning electron microscopy and X-ray microanalysis*, **1987**.
- [10] <http://www.uwo.ca/fab/equipment/analysis/1540XB.html>
- [10] T. E. Everhart, and R. F. M. Thornley, *Journal of scientific instruments*, **1960**, 37.7: 246.

- [12] J. Goldstein, et al. *Scanning electron microscopy and X-ray microanalysis: a text for biologists, materials scientists, and geologists*. Springer Science & Business Media, **2012**.
- [13] L. A. Giannuzzi, ed. *Introduction to focused ion beams: instrumentation, theory, techniques and practice*. Springer Science & Business Media, **2006**.
- [14] F. Sharifi, *Kelvin Probe Force Microscopy on Graphene Thin Films for Solar Cell and Biosensing Applications*. Ph.D. thesis. The University of Western Ontario, **2014**.
- [15] C. F. Bohren and D. R. Huffman, *Absorption and Scattering of Light by Small Particles*, Wiley, New York, **1983**.
- [16] G. Mie, *Annals of Physics*, **1908**, 25, 377.

Chapter 3

3 Theoretical methods

For the theoretical calculations, we employed a tight-binding model to deduce the electronic band structure and the formation energy of graphene decorated with Cu atoms. The electronic wave functions of metallic atoms absorbed on graphene show modifications of π -bonds in the immediate vicinity of the metallic atoms without altering the bond structure of graphene or producing any significant lattice distortions [1]. Thus, we can understand the influence of Cu atoms on graphene in our model by modifying the interaction energy of the π -electron bonds for lattice sites in the immediate vicinity of Cu atoms. These affected bonds are expected to have an increased interaction energy since metallic atoms absorbed on graphene transfer a net negative charge to graphene, increasing the bond energy of the π -electron influenced by the metallic atoms.

3.1 Properties of graphene

Before introducing the theoretical model we used for our study, it is important to have an understanding of the theoretical model we used and why we chose this model. For that, more detailed discussion about the structure of graphene such as the unique band structure, and the interaction between graphene and Cu-np are presented in this section.

3.1.1 Band structure of graphene and its defect

As mentioned in chapter one, single layer graphene is a two-dimensional structure, formed by carbon atoms in a shape of a honeycomb lattice, but a more in-depth investigation at this network and its related properties require us to look at the bonding between these carbon atoms. The carbon atom possesses four valence electrons, orbiting in $2s$ and $2p$ orbitals. Also for graphene, in order to reduce the cohesion energy, one electron in an s -orbital will mix with two electrons in the p -orbital from the neighboring atoms, forming three strong covalent bonds, with an angular relation of 120° within the same plane [2-5]. This process is known as sp^2 hybridization as shown in Fig. 3. 1, while the remaining valence electrons in the p -orbital extend out the graphene plane, forming much weaker π -

bonds with neighboring atoms. These have significantly different bonding energies, compared to σ -bonds. As the in-plane σ -bonds are highly localized, the highly mobile out-of-plane π -bonds are responsible for most of the electronic properties of graphene, including the unique ‘zero bandgap’, which refers to the situation where no energy gap is present between the valence and conduction band of this hexagonal structure [6]. However, this can change when defects are present in the graphene sheet, as the hybridization of these highly mobile π -bonds in the immediate vicinity is expected to be altered, leading to a change in the electronic band structure of graphene.

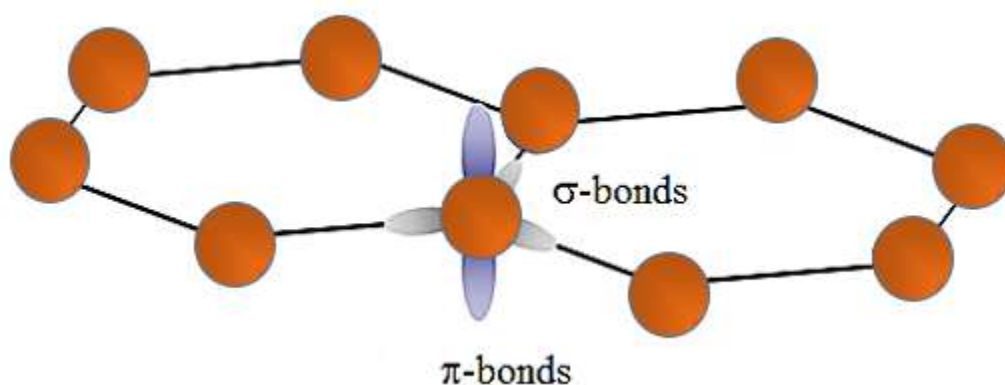


Figure 3. 1: Diagram of σ -bonds (in-plane) and π -bonds (out-of-plane) in graphene.

As far as the defect of the graphene is concerned, there are two types of defect we can take into account, structural defects and extrinsic defects. Structural defects are defects related to the structural modification of graphenes, such as vacancies, Stone-Wales defects, holes, line defects, and edges. Extrinsic defects refer to foreign atoms, such as metallic contact. Structural defects can act as the source of magnetism (single vacancies), but in this thesis, we will be more concerned with looking into the role of extrinsic defects. Graphene as a two-dimensional structure can provide a platform for the introduction of foreign species, such as atoms, and molecules. Nitrogen doping of graphene and doping graphene with metals such as Ti, Fe, and Si atoms or metal nanoparticles have attracted great attention [7-9], but in our thesis, copper nanoparticles are studied.

As discussed in Chapter 1, decorating the surface of graphene with metal atoms can serve as a method for doping graphene without dramatically altering its bond and geometrical structure. On the one hand, metal atoms decorated on the surface of graphene act as electron donors. On the other hand, metallic contacts absorbed on graphene can act as either acceptors or donors depending on the metal. Additionally, absorption of some metal contact (such as Co, Ni and Pd) on graphene significantly alters the bonds and electronic structure of graphene by forming chemical bonds, while for other metals (e.g. Al, Cu, Ag, Au, and Pt) only weak van der Waals type forces between graphene and the metal contact take place, preserving the bond structure of graphene [10]. Hence, the preservation of the bond structure when decorating the surface of graphene with metal atoms allows us to implement a simple tight-binding model to describe the electronic properties of the system.

3.1.2 Graphene edge chirality

Typically, chirality can be associated with the edges in graphene nanoribbons [11-13]. However, a clear dependence of the formation of our impurity line features and superlattices along the armchair edges has been observed, as discussed in the later chapter. This suggests that useful comparison can be made by simulating the formation energies of Cu-np arrays along both armchair and zigzag edges, therefore leading to an interpretation of this self-assembly.

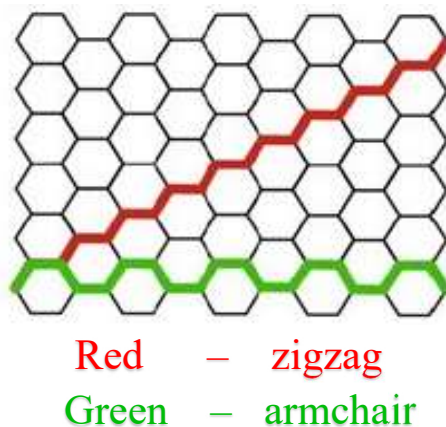


Figure 3. 2: Honeycomb lattice of Graphene at different directions: zigzag (red) armchair (green).

As shown in Fig. 3. 2, depending on the shape of the edges, they can be categorized into two types, armchair, and zigzag. For our case, lines of Cu-np's typically align along armchair edges and crystallographic directions of a graphene flake. These are normally more naturally abundant than their zigzag counterparts because armchair formation has a slightly lower surface energy level than the zigzag formation [11]. Usually, armchair edges form angles of 60° , and in the case of zigzag edges, angular relations of 120° would be seen.

3.2 Theoretical model of graphene

As we mentioned, π -electrons have high mobility out of the graphene plane and govern most of the graphene electrical properties, while the σ -electrons are highly localized. These two orbitals are effectively decoupled, which allows us to deal with the calculations of the two independently. As the bonds between graphene and Cu are weak, the band structure of graphene is not significantly altered, allowing us to employ a tight binding model based on the pristine graphene model, with additional modifications due to influence by Cu atoms. In this section, a brief introduction is given to the tight-binding model as used by A. Akbari-Sharbat for calculating the electronic properties of graphene influenced by the presence of Cu-np [1, 14] in the second quantization basis.

3.2.1 Tight-binding model

The tight-binding model (or TB model) is an approach to the calculation of electronic band structure using an approximate set of wave functions based on the superposition of wave functions for isolated atoms located at each atomic site. In the case of graphene, a lattice with the periodic placement of atoms is constructed into a honeycomb pattern. The full Hamiltonian in the vicinity of each lattice is approximated by using the isolated Hamiltonian of the isolated atom H_{at} at that site. Hence, Hamiltonian H_{at} and the wave functions Ψ_n are localized for each individual atom. Thus at each lattice site, we can write the following eigen function equation

$$H_{at}\Psi_n = E_n\Psi_n, \quad (3.1)$$

where E_n is the energy eigenvalue of the n^{th} atomic orbital. In this basic form, a correction potential $\Delta U(\vec{r})$ to the Hamiltonian needs to be introduced as follows since Eqn. 3.1 does not account for the neighboring atoms in solids. So after $\Delta U(\vec{r})$ is added, the full Hamiltonian of the becomes

$$H = H_{at} + \Delta U(\vec{r}). \quad (3.2)$$

Usually, $\Delta U(\vec{r})$ is treated as a perturbation which includes all corrections to produce the entire landscape in atomic potential of the crystal. In a realistic case, $\Delta U(\vec{r})$ would become small in regions where Ψ_n is non-zero and its wave function is expected to deviate from the atomic form. The modified wave functions can be represented as

$$\phi(\vec{r}) = \sum_n a_n \Psi_n(\vec{r}), \quad (3.3)$$

with a_n as the wave function coefficient at the n^{th} orbital. Now we can rewrite the time independent Schrödinger equation for the graphene crystal with a new notation of eigenvalue that has \vec{k} dependence as

$$H\Psi(\vec{r}) = [H_{at} + \Delta U(\vec{r})] \Psi(\vec{r}) = \varepsilon(\vec{k})\Psi(\vec{r}). \quad (3.4)$$

Here the contribution from the $\Psi_m(\vec{r})$ to the total energy can be calculated from the following integral

$$\int \Psi_m^*(\vec{r})H\Psi(\vec{r}) d\vec{r} + \int \Psi_m^*(\vec{r})\Delta U(\vec{r}) \Psi(\vec{r}) d\vec{r} = \int \Psi_m^*(\vec{r})\varepsilon(\vec{k}) \Psi(\vec{r}) d\vec{r}. \quad (3.5)$$

Substituting Eqn. 3. 1 into Eqn. 3. 5 eventually yields

$$(\varepsilon(\vec{k}) - E_m) \int \Psi_m^*(\vec{r})\Psi(\vec{r}) d\vec{r} = \int \Psi_m^*(\vec{r})\Delta U(\vec{r})\Psi(\vec{r}) d\vec{r}. \quad (3.6)$$

So, for a system with more than one site, the wave function is just the superposition of N sites. As a periodic structure, it should obey Bloch boundary condition [15, 16], so the eigenfunction of the crystal Hamiltonian should have the form of a plane wave times a function with the periodicity of the Bravais lattice. Specifically, we have

$$\Psi_{\vec{k}}(\vec{r}) = \sum_i^N e^{i\vec{k}\cdot\vec{R}_i} \phi(\vec{r} - \vec{R}_i), \quad (3.7)$$

where \vec{k} is the wave vector associated with the crystal, and \vec{R}_i is the position of the i^{th} lattice site. According to orthogonality condition, we have

$$\int \Psi_m^*(\vec{r})\Psi(\vec{r}) d\vec{r} = \delta_{n,m}. \quad (3.8)$$

Further manipulation obtained by substituting the wave function Eqn. 3. 7 into Eqn. 3. 6 using the Eqn. 3. 8 produce

$$\begin{aligned} & (\varepsilon(\vec{k}) - E_m) \left[a_m + \sum_n a_n \sum_{R_i \neq 0} a_{m,n}(\vec{R}_i) e^{i\vec{k}\cdot\vec{R}_i} \right] \\ &= \sum_n a_n \beta_{m,n} + \sum_n a_n \sum_{R_i \neq 0} \gamma_{m,n}(\vec{R}_i) e^{i\vec{k}\cdot\vec{R}_i}, \end{aligned} \quad (3.9)$$

where

$$a_{m,n}(\vec{R}_i) = \int \Psi_m^*(\vec{r})\Psi_n(\vec{r} - \vec{R}_i) d\vec{r}, \quad (3.10)$$

$$\beta_{m,n} = \int \Psi_m^*(\vec{r})\Delta U(\vec{r})\Psi_n(\vec{r}) d\vec{r}, \quad (3.11)$$

$$\gamma_{m,n}(\vec{R}_i) = \int \Psi_m^*(\vec{r})\Delta U(\vec{r})\Psi_n(\vec{r} - \vec{R}_i) d\vec{r}. \quad (3.12)$$

With the assumption that we have localized atomic orbitals on each lattice site, we expect a , γ , and product of ΔU and Ψ are always to be small. This would therefore result in $\varepsilon(\vec{k}) = E_m$ when a_m is large, and $\varepsilon(\vec{k})$ very much different than E_m when a_m is small, according to Eqn. 3. 9. Consequently, only when the coefficient a_m is equal or close to energy E_m would it contribute appreciably to the crystal wave function. So when E_m is non-degenerate, for an s -orbital, we apply the condition $|a_{m,n}(\vec{R}_i)| \ll 1$, and Eqn. (3. 9) reduces to the s -band dispersion relation

$$\varepsilon(\vec{k}) = E_m + \beta_{m,n} + \sum_{R_i \neq 0} \gamma_{m,n}(\vec{R}_i) e^{i\vec{k}\cdot\vec{R}_i}, \quad (3.13)$$

where $\beta_{m,n}$ is the correction term to E_m due to the potential ΔU , and it can be interpreted as the ionization energy or the local work function of the crystal. The first two terms above correspond to the onsite energy eigenvalue of the full crystal Hamiltonian, while the last term is the propagation term describing the interaction energy between neighbouring lattice sites multiplied by a propagating plane wave.

Equivalently, Eqn. (3. 13) can be written in a second quantization form [17]. In this case the modified tight-binding Hamiltonian in the s -band approximation in terms of creation and annihilation operators is

$$H = \sum_i \varepsilon_i c_i^\dagger c_i + \sum_{i,j} t_{i,j} c_i^\dagger c_j \quad (3. 14)$$

where c^+ (c) indicate the creation (annihilation) operators, ε_i is the ionization energy of the π -electron at lattice site i , and $t_{i,j}$ is the hopping integral [18] between sites i and j taken to be nonzero between nearest neighbor sites.

3.2.2 Modified tight binding model for impurities

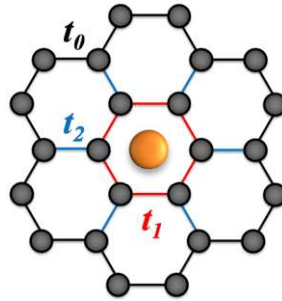


Figure 3. 3: Hopping parameters in the presence of metal atoms on graphene, under the assumption that the six C atoms forming the central hexagon on the graphene lattice directly interact with the metal.

The presence of a metal atom on a graphene surface is expected to alter the hybridization of π -electrons in the immediate vicinity of the metal atom. This leads to a modified ionization energy and hopping integral for the affected sites. Fig. 3. 3 depicts a metal atom located at the center of a hexagon on the graphene lattice. Due to the short-range nature of the electronic wave functions, the π -electron bonds most affected by the presence of the

metal atom are modeled. The C=C bonds in which both C atoms interact with a Cu atom (red) and to a lesser extent the C=C bonds in which only one C atom interacts with a Cu atom (blue) may also be affected in terms of hopping parameters. Specifically, we here utilize $t_0 = 2.90$ eV (as customary for unperturbed C=C bonds [1, 2]) and $t_1 = t_0$ and $t_2 = 1.5t_1$ as recently proposed to successfully reproduce the same results of the Kelvin probe force measurements in graphene materials decorated by Cu nanoparticles [14].

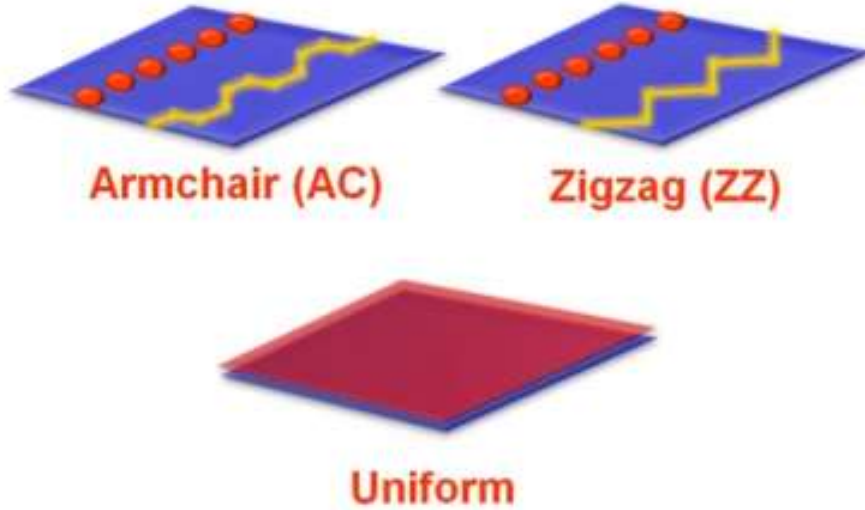


Figure 3. 4: Simulations of single arrays of Cu along armchair (AC) and zigzag (ZZ) directions of a graphene lattice as well as for a uniform copper distribution with Cu:C = 1:8.

Using the SHARCNET computer network for our simulations, we adopted the single-layer graphene structure as an approximation for our study. A Hamiltonian matrix of a graphene flake of 29×29 aromatic rings were conveniently constructed (see Ref. [14] for details). In our model we qualitatively use Cu atoms for the calculation, assuming that these atoms occupy the central spot of the hexagon, which introduces a modified local potential ΔU_{mod} for sites in contact with the atoms. As indicated in Eqn. 3. 14, the modified potential changes the diagonal ε_i and off-diagonal $t_{i,j}$ matrix elements. We denoted the modified diagonal as ε_{mod} and the modified off-diagonal matrix elements as t_{mod} , whereas the unaffected work function and nearest-neighbor interaction energy of graphene of the sites are labeled as ε_0 and t_0 respectively. Due to the introduction of the modified potential ΔU_{mod} , a shift in the highest occupied molecular orbital (HOMO) for sites in contact with

Cu atoms would occur. The changes in the work function of graphene as a consequence of these changes in the local work function of graphene were subsequently deduced.

In our study different configurations were attempted under the scenario that these configurations should always have the same overall amount of Cu atoms on them. Simulations were made of uniformly distributed Cu atoms on graphene (see more details in Chapter 5), arrays along an armchair direction, and arrays along a zigzag direction, as shown in Fig. 3. 4.

3.3 Conclusion

In this chapter, a basic introduction to the equations used in the theoretical growth model was given, meanwhile, a reference to Ref. [14] for additional information was made. As the tight binding model for pristine graphene was constructed and used qualitatively for our graphene thin films, later modifications to the local potential for sites were introduced to the system to approximate the effect of Cu-np on this graphene structure. Applications will be discussed in Chapter 5.

3.4 Reference

- [1] A. Akbari-Sharbaf, S. Ezugwu, M. S. Ahmed, M. G. Cottam, and G. Fanchini, *Carbon*, **2015**, 95, 199-207.
- [2] A. K. Geim, and K. S. Novoselov, *Nature materials*, **2007**, 6, 183.
- [3] A. K. Geim, *Science*, **2009**, 3, 1530.
- [4] A. H. Castro Neto, F. Guinea, N. M. R. Peres, K. S. Novoselov and A. K. Geim, *Rev. Mod. Phys.* **2009**, 81(1), 109.
- [5] M. J. Allen, V. C. Tung and R. B. Kaner, *Chem Rev.* **2009**, 110(1), 132.
- [6] J. Robertson, E. P. O'Reilly, *Phys. Rev. B*, **1987**, 35(6), 2946.

- [7] K. Pi, K. M. McCreary, W. Bao, Wei Han, Y. F. Chiang, Y. Li, S.-W. Tsai, C. N. Lau and R. K. Kawakami, *Phys. Rev. B*, **2009**, 80, 075406.
- [8] H. Wang, T. Maiyalagan and X. Wang, *ACS Catal.* **2012**, 2(5), 781.
- [9] W. Zhou, M. D. Kapetanakis, M. P. Prange, S. T. Pantelides, S. J. Pennycook and J.-C. Idrobo, *Phys. Rev. Lett.* **2012**, 109, 206803.
- [10] G. Giovannetti, P. A. Khomyakov, G. Brocks, V. M. Karpan, J. Van den Brink and P. J. Kelly, *Physical Review Letters*, **2008**, 101, 026803.
- [11] F. Cervantes-Sodi, G. Csányi, S. Piscanec and A. C. Ferrari, *Phys. Rev. B*, **2008**, 77, 165427.
- [12] Z. F. Wang, Q. Li, H. Zheng, H. Ren, H. Su. Q. W. Shi and J. Chen, *Phys. Rev. B*, **2007**, 75, 113406.
- [13] E. Cruz-Silva, Z. M. Barnett, B. G. Sumpter and V. Meunier, *Phys. Rev. B*, **2011**, 83, 155445.
- [14] A. Akbari-Sharbaf, *Defect-Related Magnetic and Electronic Properties of Graphene*. Diss. The University of Western Ontario, **2014**.
- [15] M. G. Cottam and D. R. Tilley, *Introduction to Surface and Superlattice Excitations*, 2nd edition, IOP **2005**.
- [16] N. W. Ashcroft and N. D. Mermin, *Solid State Physics*, Brooks/Cole, **1976**.
- [17] J. J. Quinn and K.-S. Yi, *Solid State Physics: Principles and Modern Applications*, Springer, **2009**.
- [18] T. D. Schultz, *Quantum Field Theory and the Many-body Problem*, Gordon and

Breach, 1964.

Chapter 4

4 Parametric study in superlattices fabrication and its evanescent waveguiding properties

Using SEM as the primary way to image the morphology of the superlattices, it was found that the spontaneous formation followed a certain trend: in the beginning of the process, small Cu-np aggregated and formed larger particles while aligning into periodic arrays, gaining uniformity in the particles' size and periodicity in the inter-particle spacing, however as the process continued, the formed superlattices started to deform due to excessive heat and eventually became randomly distributed Cu-np on graphene. Despite the fact that the role of time and temperature are different, it was observed in our study that the formation with the highest periodicity was usually achieved under an annealing temperature at 360°C regardless of the annealing time.

Hence, in the first half of this chapter, the role of the annealing temperature and time will be discussed centering the experimental results from the 360 °C as a reference of our superlattices, compared to samples obtained from other conditions with lower periodicity. Cu-np angular features and other secondary patterns such as curving are briefly discussed. As for the second half of this chapter, results and interpretation for the investigation of the evanescent waveguiding properties of our superlattices are presented.

4.1 Parametric study of superlattices forming conditions

In our study, to maximize the periodicity of Cu-np lines, we investigated possible factors during our fabrication by conducting control experiments. A set of samples annealed under different conditions as described in Chapter 1, revealing the role of the annealing temperature and time. As the best results were obtained repeatedly under the condition at 360°C and 8 hours, the following discussion will expand around this condition.

4.1.1 Role of annealing temperature

Fig. 4. 1 demonstrates the role of temperature in the formation of superlattices of Cu-np from low temperature to high temperature.

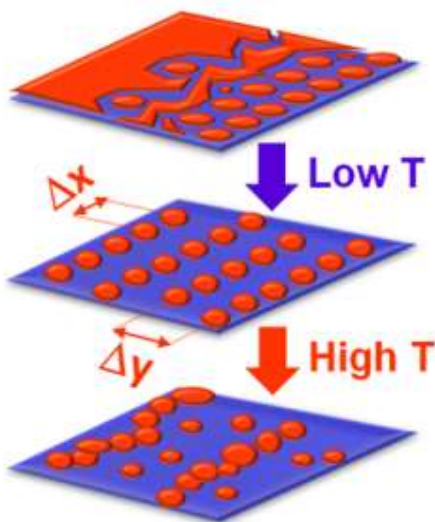


Figure 4.1: A diagram illustrating the different behavior of Cu-np's nucleated at different temperatures is also provided, showing a trend from semi-continuous and nano-structured Cu layers at the lowest temperatures to sparse assemblies at the highest temperatures, with superlattices forming at intermediate temperatures.

In Fig. 4. 2, two SEM images are shown at each temperature condition. It can be observed that at the lowest annealing temperature (200°C), the formation of ordered structures is rare, a slightly more mature formation can be seen in the proximity of graphene flake edges (panel a). But more often, copper nucleation is typically very limited at such temperatures [1, 2] and produces semi-continuous films of interconnected nano-structures (panel b). As the temperature increases (280°C), the structure of multiple parallel Cu-np's lines become obvious, but Cu-np's are still in the process of nucleation, individual Cu-np's are nucleating into certain sites along the lines (panel c) or between the lines (panel d), but have yet to merged with others.

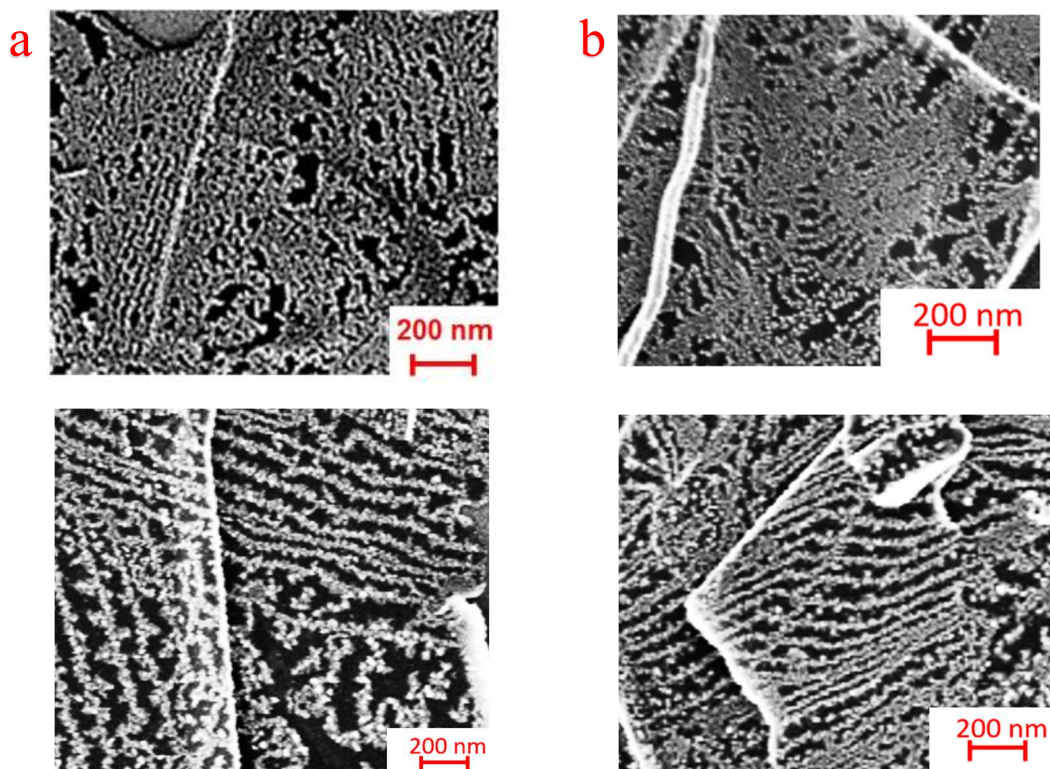


Figure 4. 2: SEM images of samples annealed for 8 hours at low temperatures: (a) and (b) 200 °C, Cu layer remains in a semi-continuous state. (c) and (d) 280 °C, Cu-np lines feature has emerged, but superlattice with constant interline and interparticle spacing has not yet formed.

The ideal annealing temperature appears to be higher, as in Fig. 4. 3 at about 360 °C, at which ordered superlattices of Cu-np's at 18 ± 4 nm diameter can be found. At 360°C and 8

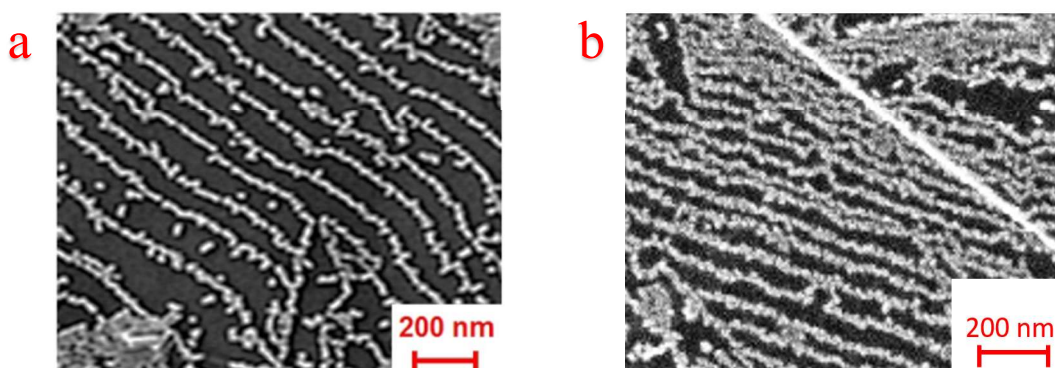


Figure 4. 3: SEM images of samples annealed for 8 hours at ideal temperatures: (a) and (b) 360 °C, superlattice with constant interline and interparticle spacing is established.

hours (panel a, b) Cu-np's align well along lines parallel to the armchair direction of the graphene lattice, with relatively low ($\Delta x = 12 \pm 3$ nm) inter-particle spacing, while the spacing between lines ($\Delta y = 182 \pm 6$ nm) is significantly higher.

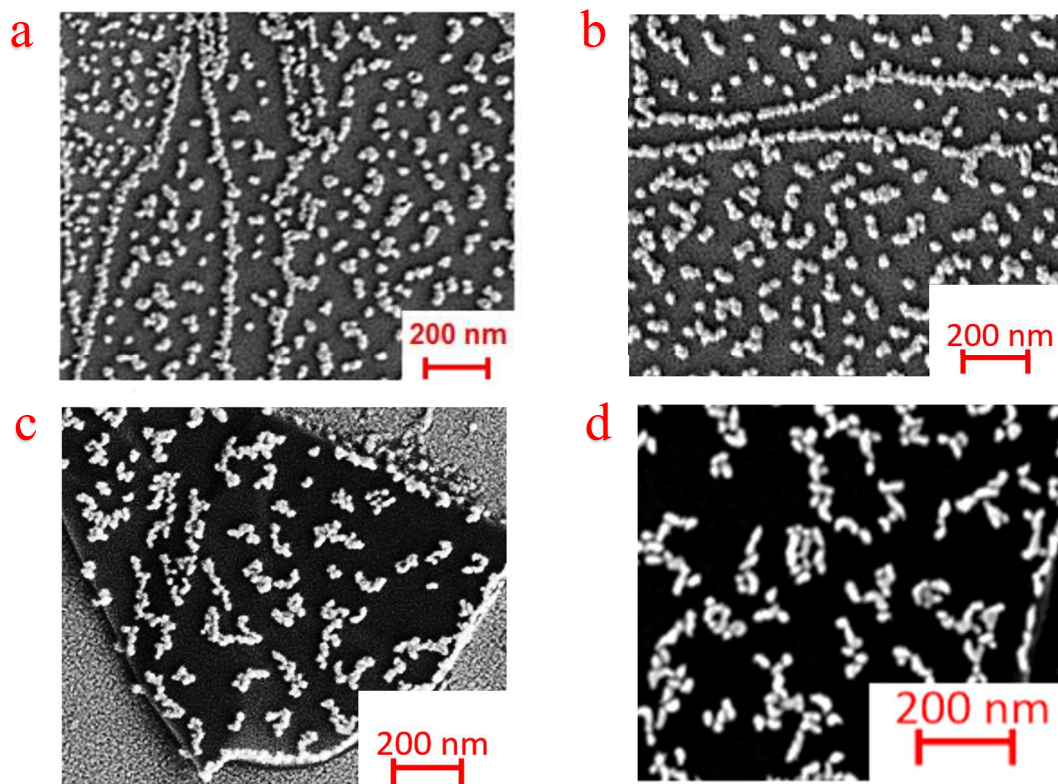


Figure 4. 4: SEM images of samples annealed for 8 hrs. at high temperatures: (a) and (b) 440 °C, high temperature causes Cu-np to further nucleate, forming larger Cu-np's. (c) and (d) 480 °C, Cu-np disorderedly distributed has become the most common feature and lines feature is very rare.

When the temperature goes higher (440 °C), Ostwald ripening occurs, mostly from particles that become displaced from their preferential superlattice sites due to kinetic effects. Consequently, Cu-np lines are significantly lowered in number, and significantly deformed, and commonly, the separation between lines is either widened (panel a, Fig. 4. 4) or narrowed (panel b, Fig. 4. 4). At an even higher temperature, Cu-np tends to aggregate but yet to condense into individual particles, as in panel c and d. We suspect that, even at the lowest annealing temperatures, nucleation of Cu-np's mostly occurs when the Cu thin

layer is in the molten state, since the melting temperature of metallic nanoparticles and ultrathin metallic films of only a few atomic layers is significantly lower than in the corresponding bulk metal [3]. When the characteristic size of the ripening particles becomes large enough to solidify them at that specific annealing temperature, the nucleation process ends, resulting in their random distribution over a relatively large area.

4.1.2 Role of annealing time

Fig. 4. 5 explores the role of annealing time in the formation of superlattices from a short time to a long time.

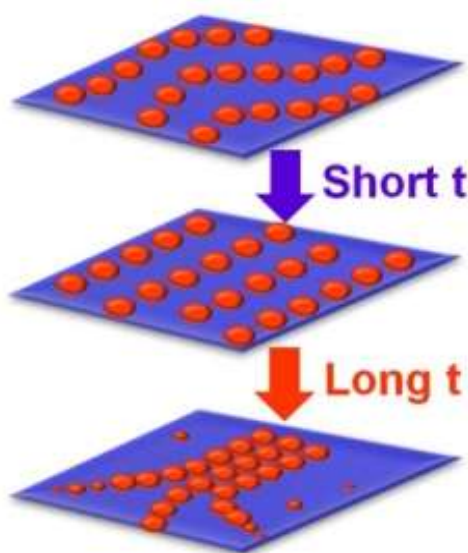


Figure 4. 5: Diagram illustrating the different behavior of Cu-np's self-assembly at different times, showing a trend from curved lines of Cu-np's at relatively constant distances Δy at the shortest times to isolated and coalescing lines of Cu-np's at the longest times, with superlattices forming at intermediate times.

In Fig. 4. 6, two SEM images are shown at each time condition. A short duration of annealing (1 hour) will initiate a preliminary stage of the nucleation, the Cu-np's film starts to crack (panel a, b) due to movement of Cu-np, but no significant pattern is established. As the duration increases (3 hours), nucleation that leads to the formation of some small Cu-np has taken place, yet continuous layer adhering to these particles (panel c) and regional disorder (panel d) remain to be the dominant features. Constant interline spacing

Δy is established at relatively short annealing times (5 hours), but significant imperfections in the superlattices are due to the fact that, not infrequently, arrays of Cu-np's are actually parallel curved lines if too short annealing times (panel e), also, noticeable variation in spacing is observed (panel f) at this stage.

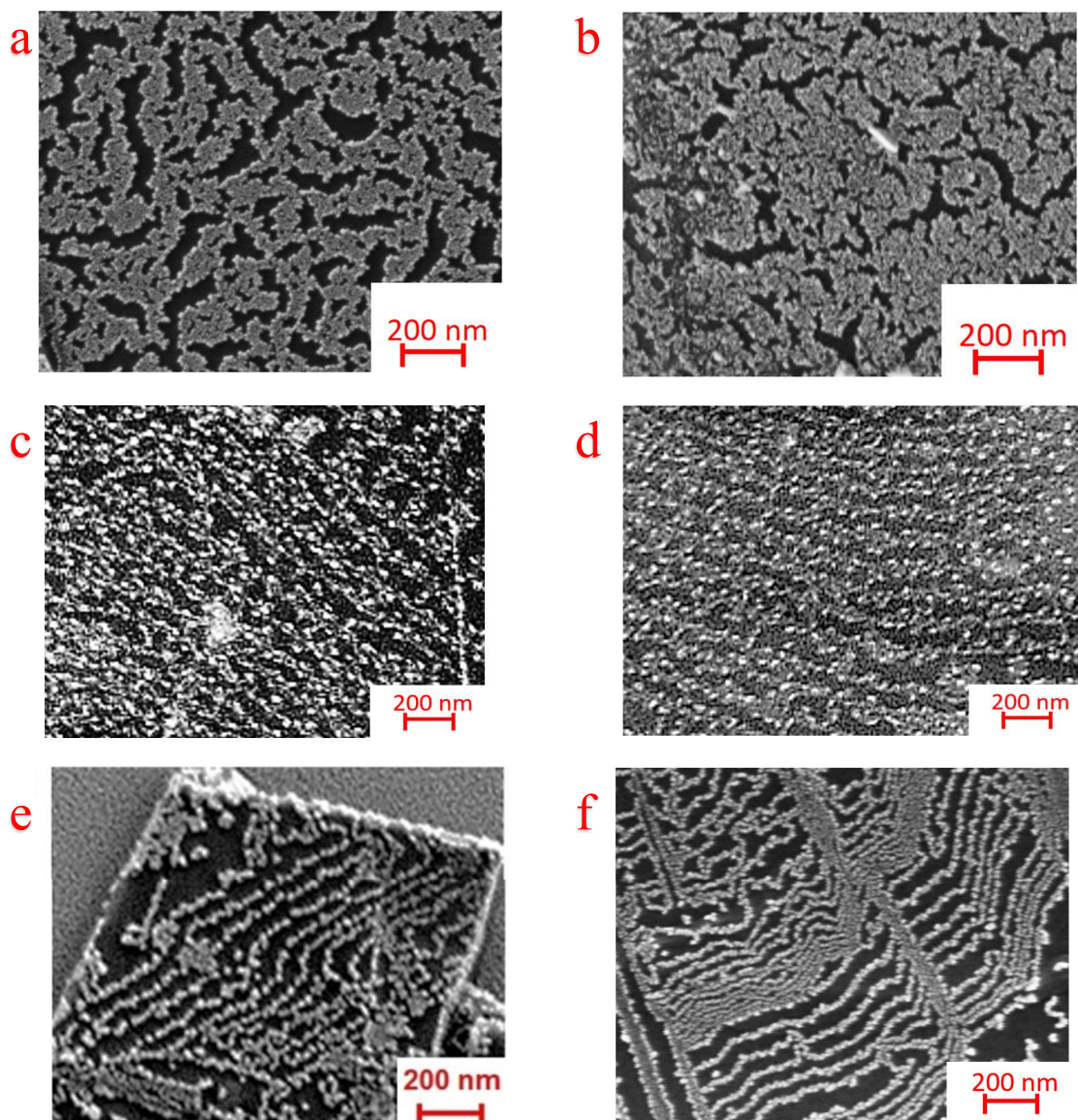


Figure 4. 6: SEM images of samples annealed at 360°C at short times (a) and (b) 1 hour, (c) and (d) 3 hours, and (e) and (f) 5 hours. It can be observed that, short annealing only prompts the Cu-np's to form into lines feature, but not superlattice.

At the optimal conditions of about 8 hours, superlattices with uniformly distributed and remarkably straight lines of Cu-np's are formed, with an interline lattice spacing $\Delta y =$

186±6 nm at 360°C, as shown in panel a and b in Fig. 4. 7. At longer times (e.g. at 12 hours at 360°C), the progressive coalescence of nearest-neighboring lines of Cu-np's becomes the dominant process. Consequently, exceedingly long annealing times result in graphene platelets relatively free of Cu-np's, with many isolated lines of Cu-np's tending to converge into one, as shown in panel c, in the meantime, Cu-np become sparser (panel d), which is mostly likely due to at this temperature, small Cu-np have aggregate and melt into larger particles. With the understanding of the role of temperature and time, attempts to reproduce superlattices with relatively small fluctuations of the annealing temperatures and times about 360°C and 8 hours can lead to the possibility to design superlattices with different lattice parameters, Δx and Δy .

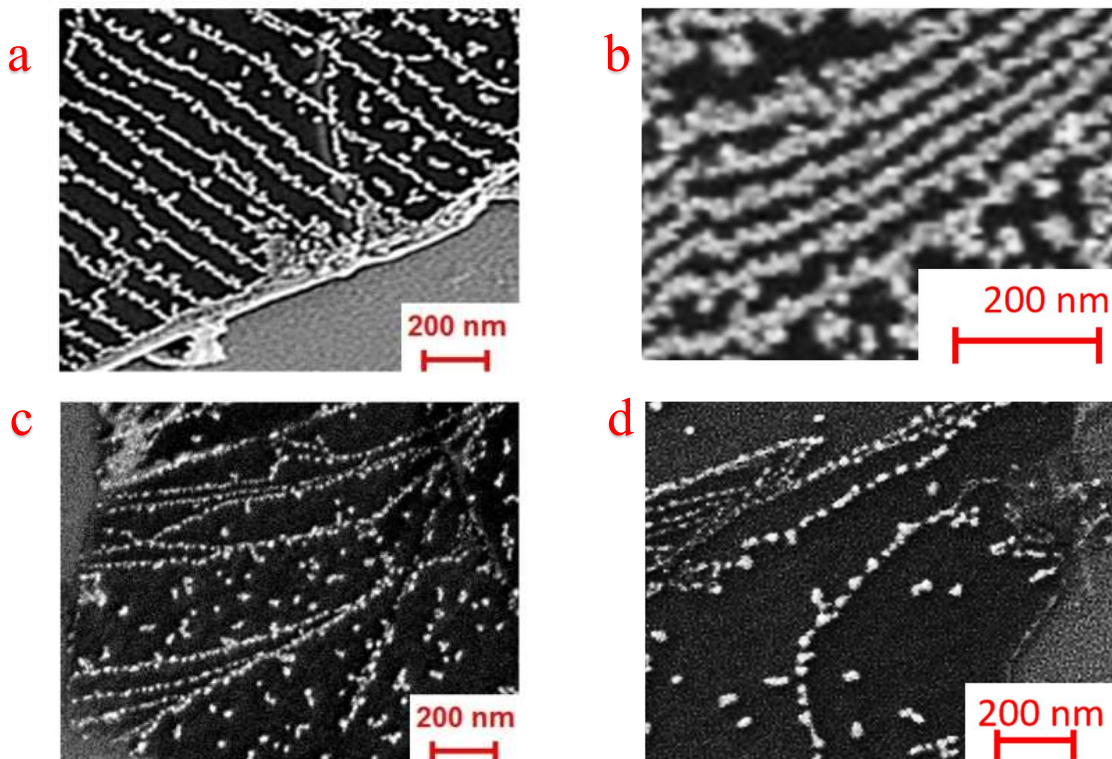


Figure 4. 7: SEM images of samples annealed at 360°C at ideal times (a) and (b) 8 hours, superlattice with constant interline and interparticle spacing is established. And long times (c) and (d) 12 hours, nucleation of Cu-np tends to happen faster at certain sites, resulting in the merging of lines at one ends.

4.2 Secondary Cu-np features

Concerning the fabrication of the superlattices, the main purpose is to obtain alignment of periodic arrays of Cu-np on graphene thin film, yet usually, other patterns also occurred repeatedly during the fabrication. While an appropriate condition prompts the spontaneous formation, other factors induced by the properties of the underlying graphene also have influence on the fabrication. These factors, such as number of layers and the flatness, are yet to be discussed. Understanding these Cu-np features could be the key to our understanding of the formation of the superlattices. In this section, several secondary self-assembled patterns are presented and discussed.

4.2.1 Parallel curving of Cu-np

As the most common secondary pattern, curving can be found due to several reasons. Apart from the scenarios described above, where immature formation due to insufficient annealing time and excessive annealing that leads to union of adjacent Cu-np's lines, spontaneous arrangement also takes place in the fashion of parallel curving when certain structural features (topographical edges) of the underlying graphene platform are present. As shown in Fig. 4. 8, parallel curved lines are found at the right end of the image, which is an evidence that it is the edges of a graphene flake where we find these curving the most.

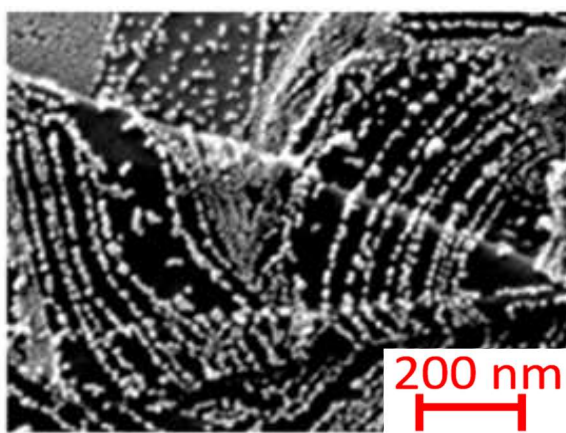


Figure 4. 8: SEM micrograph of curved lines of Cu-np's formed at 360°C for 5 hours, underlying graphene provides a topographical edge for the nucleation, resulting in curved Cu-np lines.

4.2.2 Angles and preferable direction of alignment

Not limited to curving, angular features are also observed along these edges. Interestingly, such feature usually occurs when parallel lines start to surface during the nucleation, it maintains such direction until excessive annealing destroys the periodicity. When angular features are present, most commonly, it appears to be either two separate groups of Cu-np's lines intersecting with each other or one single group of lines bending in the vicinity of the edge. In either case, an angular relation of around 60° or 120° is typically observed, as shown in Fig. 4. 9. These arrangements are mostly associated with the underlying graphene structures, which opens up the opportunity for understanding the self-assembly of our superlattices.

For graphene, as mentioned in Chapter 3, the honeycomb lattice structure possesses two chiral directions: armchair and zigzag [4-6]. In our observation, lines of Cu-np's align along the intersection of two armchair edges of a graphene flake, indicated by angles of 60° or 120° and 180° , as opposed to the intersection of an armchair and zigzag edge, which is normally indicated by angles of 30° or 90° between two boundaries. The angular features can be attributed to the self-assembly when Cu-np nucleate into parallel lines near the intersection of two armchair edges and form certain angles, most commonly armchair angles. This gives us a good indication of the possible forming mechanism of superlattices associated with the formation energy along the armchair edges of the underlying graphene, which leads to the theoretical simulation in Chapter 5.

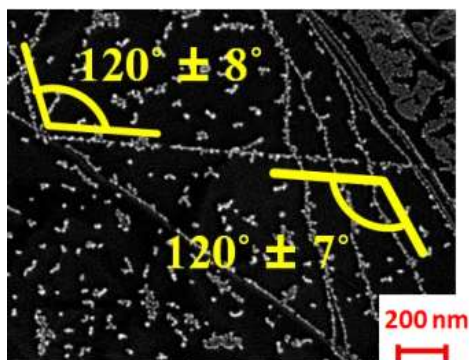


Figure 4. 9: SEM image obtained from sample annealed at 500°C annealing showing Cu-np's lines along armchair edges of graphene domains.

4.2.3 Arrays of unevenly spaced lines of Cu-np

Another type of defect is array with variable separation. From the section above, it is known that to obtain well-formed superlattices, fine control of the annealing condition is crucial. The fluctuation in the in the periodicity of lines separation are mostly associated with a combination of annealing conditions and the underlying graphene structures. In Fig. 4. 10, separation of $\Delta y = 200 \pm 11$ nm at the highest and $\Delta y = 15 \pm 4$ nm can be found. Differed from the case of the excessive duration of annealing, these type of arrangements maintain the straightness of individual lines. While the aggregation due to annealing of particles clearly took place judging from the Cu-np of bigger size on the left side of the image, the flatness of the underlying structure could play a role as well. As this aggregation only happened partially on the sample, it could be due to the fact that, the underlying thin films are not uniform in these particular cases, which generates temperature difference at different regions, hence the relatively early deformation and aggregation of lines compared to other spots that are still at a facilitating temperature for the formation of Cu-np's lines.

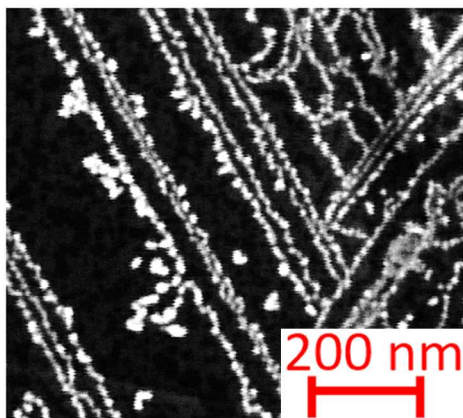


Figure 4. 10: SEM image obtained from sample annealed at 335°C and 8 hours showing Cu-np's lines with variable separation (a clear angular feature is also observable).

4.3 Evanescent waveguiding properties

To show the evanescent waveguiding properties, a demonstration of evanescent waveguiding in Cu-np's superlattices, as opposed to isotropic Mie scattering in regions of non-aligned Cu-np's, is offered in Fig. 4. 11. The region in the AFM topography image in

panel a corresponds to the reflection-collection mode SNOM image shown in panel b, in which a brighter pixel represents a higher intensity of scattered light being collected at that point in the close proximity to the sample. Since AFM is not capable of resolving our superlattices, we obtained a SEM image of the same location (panel c) using FIB markers. It clearly shows that a superlattice with lines of Cu-np's parallel to the light propagation direction (which is vertical, along the Y-axis, in Fig. 4. 11a-c) exists at section A-A'. Conversely, SEM shows that Cu-np's distribution is less ordered, and not parallel to the light propagation direction, in the sample cross section labeled as B-B' in Fig. 4. 11a-c. Consequently, an (Y, Z) scan along section A-A' is expected to demonstrate evanescent waveguiding properties, while a similar scan along section B-B' is expected to exhibit a sequence of constructive and destructive interference patterns along the Z-axis as a consequence of incoherent Mie scattering [7, 8].

Fig. 4. 12 presents vertical SNOM scans in Z-direction for the two sections, A-A' and B-B'. Section A-A' represents an area that, in Fig 4. 11b, is significantly brighter than the surrounding regions, meaning that more light was collected from that area. This is an indication of strong light confinement since parallel lines of Cu-np's promote coherent Mie scattering with little light absorption from Cu-np's that offer a very low cross-section to the incident wave. Integrated light intensity profiles extracted from Fig. 4. 12 are reported in Fig. 4. 13 as a function of Z. For section A-A', corresponding to ordered Cu-np's superlattices, an exponential decay of light intensity in the proximity of the sample can be observed, as witnessed by the analytical exponential fit demonstrated in Fig. 4. 13 for the integrated attenuation in the A-A' cross section. Conversely, the light intensity profile for section B-B', characterized by randomly oriented Cu-np's, undergoes multiple oscillations due to the superposition of multiple and incoherent Mie scatterings in arbitrary directions. Typically, a maximum of the interference pattern at $Z_{\max} \approx \lambda$ can be predicted, with the first minimum at values of Z slightly higher than $Z_{\min} \approx \lambda/2$ [7]. These predictions compare very well of our experiments, for which we can observe, $Z_{\max} = 530$ nm and $Z_{\min} = 295$ nm from the blue trace in Fig. 4. 13. In general, oscillating light intensity profiles of this type are relatively rare in our system and confined to very disordered areas, which point at the robustness of the evanescent waveguiding properties of Cu-np's superlattices.

The evanescent waveguiding properties of our superlattices are demonstrated by the (X, Z) SNOM scan at the left side of Fig. 4. 12, corresponding to section A–A'. Along such section, confinement of the electromagnetic radiation in the bright yellow zone in the proximity of the sample surface can be observed. There is a strong attenuation of light intensity at values of Z within a few tens nm from the sample surface, which corresponds to evanescent modes. Conversely, the (X, Z) SNOM scan along section B–B' of Fig. 4. 11a–c is presented on the panel on the right side of Fig. 4. 12 and reveals a dark region in the proximity of the sample surface, with subsequent maxima and minima of scattered light intensity, due to the constructive and destructive interference of incoherent far-field modes. This is typical of relatively rare regions of our samples in which Cu-np's are disorderly

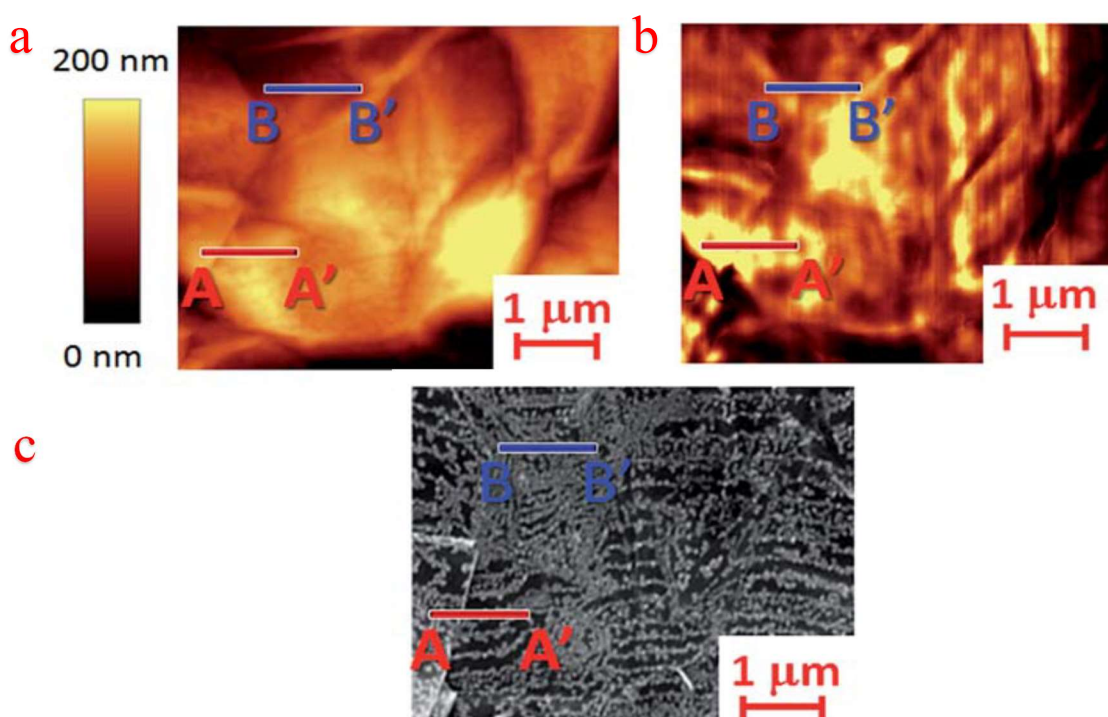


Figure 4. 11: (a) Typical AFM and (b) reflection-collection SNOM images obtained simultaneously from one of our Cu-np's superlattices annealed at 360°C for 8 hours. (c) SEM micrograph, obtained using FIB markers from the same sample region as in panels a and b. It can be observed that, AA' is between two Cu-np lines and BB' is along a region where Cu-np distributed disorderly.

distributed. The same behavior was previously observed in random arrangements of metal nanoparticles on glass [9].

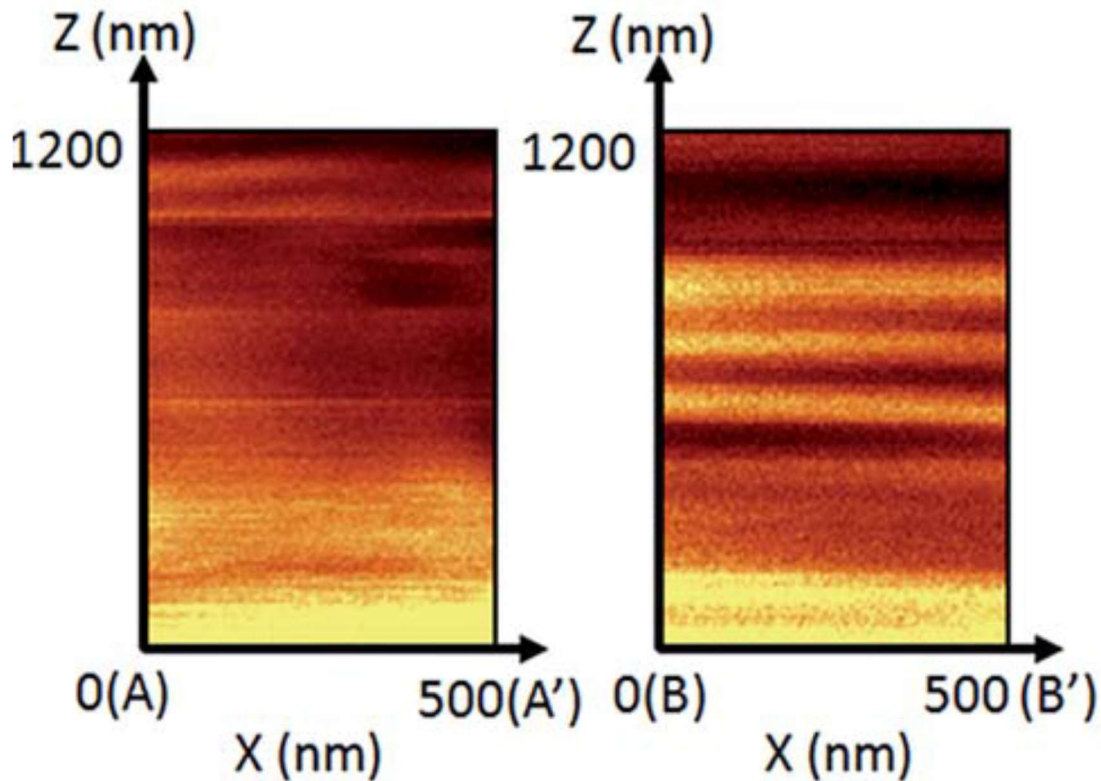


Figure 4. 12: Vertical SNOM scans in Z-direction for cross-sections indicated as A-A' (left) and B-B' (right) in Fig. 4. 11. The Z-axis extends from 0 to 1200 nm in this figure. It can be observed that, in AA' the light intensity decay gradually while in BB', additional peaks above the surface are present.

In our evanescent waveguides corresponding to ordered regions in our samples (e.g. sect. A-A' in Fig. 4. 11), the role of graphene layers is to determine the polarization of the propagating radiation. Graphene is an optical anisotropic medium with a high in-plane imaginary part of the dielectric constant ($\epsilon_{\parallel} = \epsilon_{\parallel}' + \epsilon_{\parallel}'' \approx 6+i7$ at $\lambda = 532$ nm) while the out-of-plane imaginary part of the dielectric constant is nearly zero (e.g. $\epsilon_{\perp} = \epsilon_{\perp}' \approx 3$ at $\lambda = 532$ nm) [10]. This means that unpolarised light entering graphene at grazing incidence angles will be strongly attenuated in its in-plane polarization component, while only the out-of-plane component propagating along the graphene surface. Conversely, the role of

the Cu-np's superlattice in our waveguides is in providing a preferential direction of propagation for the electromagnetic radiation, along the X-axis of the graphene surface, corresponding to the direction of the parallel lines of Cu-np's. With this architecture, the decay of the electric field along the Z-axis is determined by the interline distance between Cu-np's lines. Consequently, we expect a decay constant of the same order of magnitude of Δy , which is about 100 nm in our case. Conversely, if propagation occurred with plasmonic waveguide modes, via adjacent nanoparticles within each line, we suspect the decay constant would be significantly lower, of the order of the Cu-np's diameter, but the evanescent field intensity would also be significantly lower. However, more experiments are required to substantiate our hypothesis.

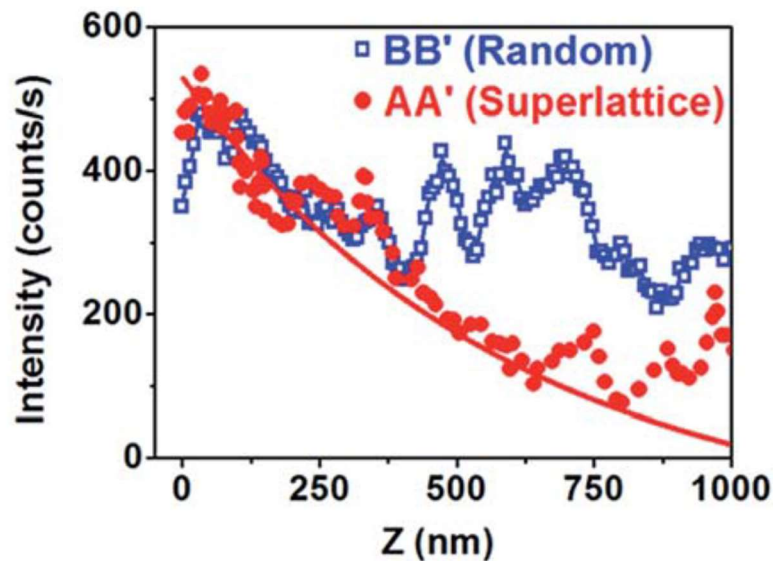


Figure 4. 13: Scans in panel d show an exponential decay of the evanescent wave mode at a distance Z from the surface for section A-A' (corresponding to a periodic superlattice). Conversely, they show random interference patterns for section B-B' (corresponding to a random distribution of Cu-np's). The red line is a fit that demonstrates the exponential decay of the evanescent mode in section A-A'.

Perhaps, the closest far-field equivalents of our near-field waveguiding superlattices are coplanar waveguides [11] consisting of parallel conducting strips of metal, equivalent to our Cu-np's lines, assembled on a dielectric substrate grown on grounded base, the equivalent of our graphene thin film on silicon. Like coplanar waveguides, our

waveguiding superlattices are most likely not supporting true transverse electromagnetic (TEM) modes because magnetic fields may have longitudinal components along the lines of our Cu-np's superlattices and electric fields may have longitudinal components at the graphene/silicon interface. Consequently, our evanescent waveguiding properties are likely of the hybrid mode, even though some similarities with TEM₀₀ modes are present.

4.4 Conclusion

In this chapter, experimental results related to the fabrication condition (during the annealing process, with the optimal result formed under 360°C for 8 hours) are presented, the role of annealing temperature and annealing time are discussed. Secondary effects occur in the vicinity of graphene edges, serve as a visual indication of the mechanism that leads to the self-assembly of our superlattices. Furthermore, data from the evanescent waveguiding experiments are presented, which suggests that our system possesses evanescent waveguiding properties for light propagating parallel to the Cu-np's lines.

4.5 References

- [1] D. Mott, J. Galkowski, L. Wang, J. Luo and C. J. Zhong, *Langmuir*, **2007**, 23, 5740.
- [2] A. K. Chawla and R. Chandra, *Journal of Nanoparticle Research*, **2009**, 11, 297.
- [3] G. Cao, *Nanostructures & Nanomaterials: Synthesis, Properties, and Applications*, Imperial College Press, London, **2004**.
- [4] F. Cervantes-Sodi, G. Csányi, S. Piscanec and A. C. Ferrari, *Phys. Rev. B*, **2008**, 77, 165427.
- [5] Z. F. Wang, Q. Li, H. Zheng, H. Ren, H. Su. Q. W. Shi and J. Chen, *Phys. Rev. B*, **2007**, 75, 113406.
- [6] E. Cruz-Silva, Z. M. Barnett, B. G. Sumpter and V. Meunier, *Phys. Rev. B*, **2011**, 83, 155445.

- [7] C. F. Bohren and D. R. Huffman, *Absorption and Scattering of Light by Small Particles*, Wiley, New York, **1983**.
- [8] G. Mie, *Annals of Physics*, **1908**, 25, 377.
- [9] S. Ezugwu, H. Ye and G. Fanchini, *Nanoscale*, **2015**, 7, 252.
- [10] S. Cheon, K. D. Kihm, H. goo Kim, G. Lim, J. S. Park and J. S. Lee, *Scientific reports*, **2014**, 4, 6so364.
- [11] M. Forman, *Asia-Pacific Microwave Conference*, **2006**, 12, 905.

Chapter 5

5 Theoretical results and discussion

We qualitatively inferred the modifications of the electronic properties of graphene associated with overlapping Cu atoms on top of them by noticing that, since metal atoms act as electron donors, an increase in both the ionization energy and hopping integral is expected [1]. Inspired by the experimentally observed armchair-oriented Cu-np's arrays, we therefore simulated the density of states and formation energy for various distributions of metal atoms on the surface of graphene, including uniformly distributed copper atoms vs. armchair-oriented copper atoms on graphene, armchair-oriented vs. zigzag-oriented copper atoms on graphene and armchair-oriented copper atoms array with different spacing. By comparing the DOS (in arbitrary unit/a. u.) we can understand which configuration has the lower formation energy and thus is more energetically favorable. The model described in Chapter 3 was employed for these calculations.

5.1 Copper atoms on graphene in uniform distribution and armchair arrays setting

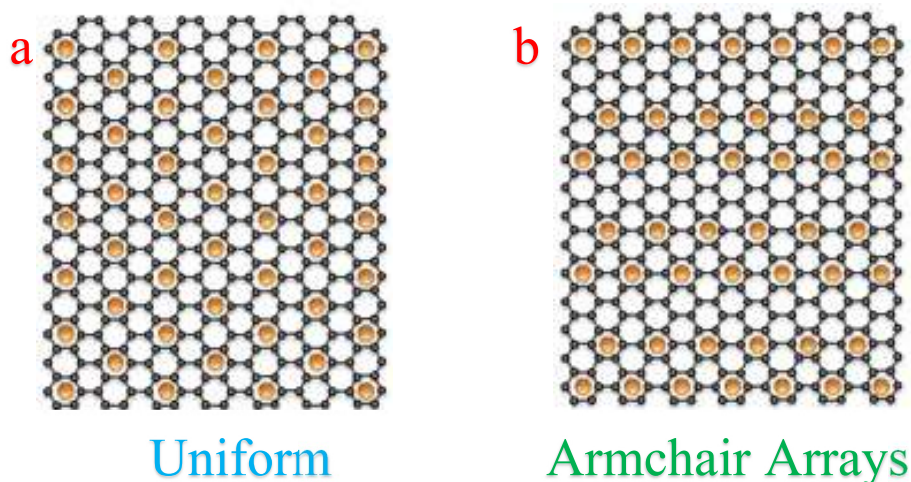


Figure 5. 1: Comparison of the density-of-states (DOS) for two different sets of distributions of Cu atoms on single-layer graphene: (a) uniform distribution and (b) arrays of Cu atoms along an armchair direction.

The self-assembly of copper nanoparticles (Cu-np's) is governed by the energy landscape of the graphene surface. We can qualitatively deduce most of the features observed in our superlattices using the modified tight-binding Hamiltonian described by Eqn. 3. 14. To illustrate the influence of Cu distribution on the formation of specific arrangements of Cu atoms that may form superlattices upon thermally-induced nucleation, we considered the formation energy of a uniform distribution of Cu atoms on graphene (Fig. 5. 1a) and we compared it to a distribution of Cu atoms consisting of a series of arrays along the armchair direction, as shown in Fig 5. 1b. In both configurations, the C:Cu atomic ratio was set equal to 8:1.

The density of π -electron bonds interacting with the Cu atoms is equal in both configurations when we set $\varepsilon_i = 0$ as in Fig. 5. 2. The setting of bare graphene is also included, labeled as NORM in black in the figure. This allows us to perform a comparison between the two structures while ensuring that the total number of bonds influenced by the metal atoms is equivalent. More accurate calculations, using both ionization energies ($\varepsilon_i = +0.5$ eV) and hopping integrals ($t_2 = 4.35$ eV) that are specific for C atoms in contact with

Cu [2] indicate (Fig. 5. 2) that the DOS for graphene with Cu atoms arranged in arrays is different from the DOS of graphene with uniform distribution of Cu atoms. The broadening of the DOS features of graphene with Cu lines reduces the formation energy of the system making this structure more energetically favorable. Our findings are consistent with DFT (density functional theory) calculations for the arrangement of other metals on graphene [3].

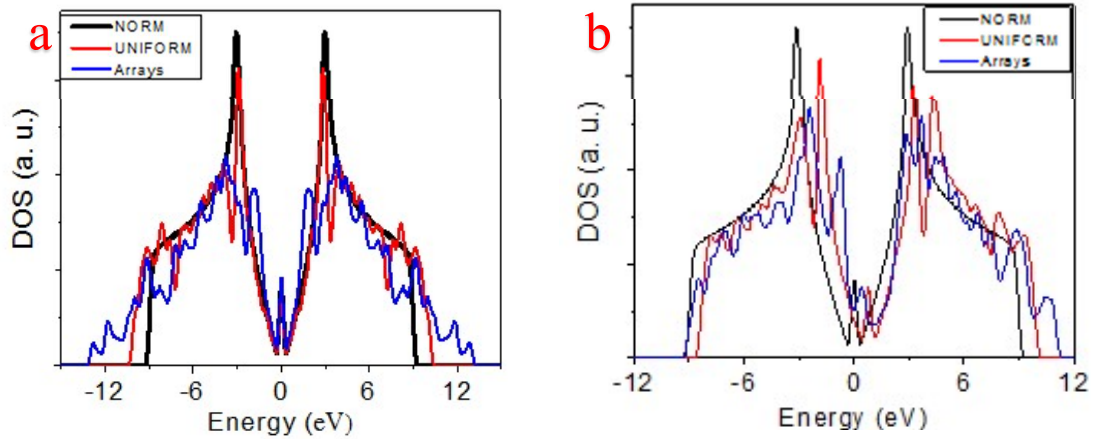


Figure 5. 2: (a) The DOS is calculated by using, in Eqn. 3. 14, the same ionization energy ($\epsilon_i = 0$) for all C atoms irrespectively of their contact or non-contact with Cu atoms. Hopping parameters $t_0 = t_1 = 2.90$ eV and $t_2 = 4.35$ eV were used. (b) The DOS is calculated by using different ionization energy ($\epsilon_i = 0$) for C atoms in contact with Cu ($\epsilon_i, \text{Cu} = +0.5$ eV). $t_0 = t_1 = 2.90$ eV and $t_2 = 4.35$ eV. It can be observed that, in both configuration, the armchair arrays distribution (blue) has the lowest DOS level.

5.2 Copper atom lines on graphene at different chiral directions

Experimental observations for our samples suggest that chains of Cu-np's form preferentially along the armchair direction of graphene, as indicated in Fig. 4. 9 and 4. 10. To validate these observations, we consider a single line of Cu atoms arranged along the armchair and zigzag directions of graphene, as shown in Fig. 5. 3. Using the same tight-binding parameters ($\varepsilon_{i, Cu} = +0.5$ eV, $t_0 = t_1 = 2.90$ eV and $t_2 = 4.35$ eV) we deduce that the formation energy of a single array of Cu atoms oriented along the armchair direction is lower than along the zigzag direction, as shown in Fig. 5. 3. The rise of the DOS feature implies a decrease in formation energy, explaining the preferential orientation of our Cu-np's superlattices at armchair direction. This result is also shown in the next section in Fig.

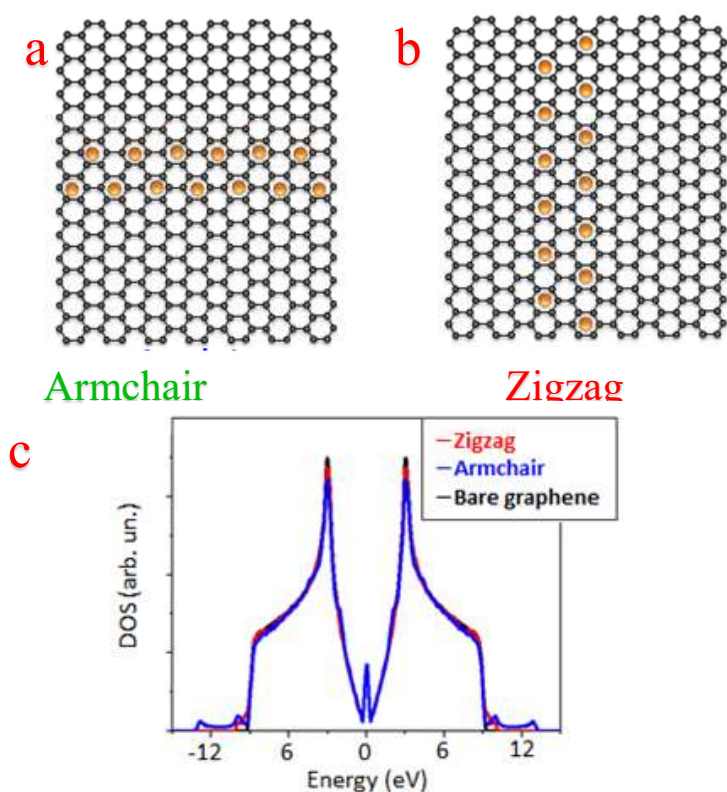


Figure 5. 3: Comparison of two different sets of arrays of Cu atoms: (a) along armchair vs. (b) along zigzag crystallographic directions of a graphene flake. (c) DOS of the armchair, zigzag and bare graphene configurations. It can be observed that, both armchair and zigzag distribution have a lower DOS level compared to bare graphene, and the armchair distribution has the lowest DOS level among the three.

5. 4a, the formation energy in an arbitrary unit of Cu-np's lines along zigzag is lower than its counterpart along the armchair direction.

5.3 Copper atoms lines on graphene at different interline distances

The interline periodicity of our superlattices could also be theoretically inferred by calculating the formation energies of parallel arrays of Cu atoms as a function of their inter-array distance Δy (Fig. 5. 4a). We find that the formation energy of parallel Cu-atom arrays depends periodically on Δy and exhibits a sequence of minima $\{\Delta y_i\}$ corresponding to preferred distances at which Cu-np's lines tend form. In special cases (Fig. 5. 4b) we could also observe a gradient in the interline spacing, with a sequence of increasingly large values of $\Delta y = \Delta y_i$ separating neighboring lines. This qualitatively explains the growth formation of Cu-np's superlattices in two steps. In the first step, a relatively uniform Cu layer resulting from thermal evaporation divides in parallel arrays of Cu atoms so that the

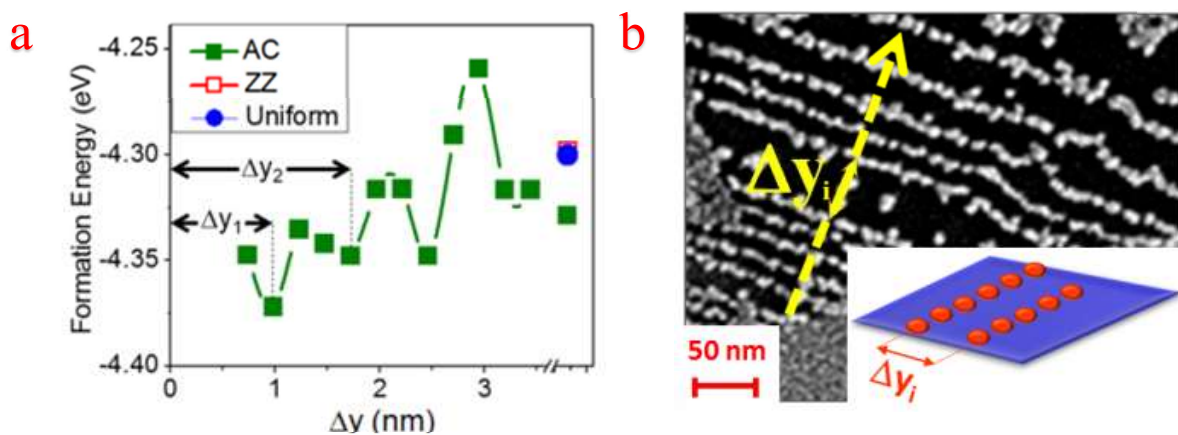


Figure 5. 3: (a) Theoretical formation energies of individual Cu-np's lines along armchair (AC) and zigzag (ZZ) directions and parallel lines of Cu-np's at interline distance Δy along AC directions. Minima for specific values of $\{\Delta y_i\}$ can be observed (with $\Delta y_1 = 1.0$ nm and $\Delta y_2 = 1.7$ nm evidenced in the plot). Each minimum corresponds to a favourable interline distance for the formation of superlattices. (b) Special case in the proximity of an armchair graphene edge, in which an irregular superlattice with multiple values of $\{\Delta y_i\}$ for parallel Cu-np's lines is shown.

interface energy of the structure reaches a local minimum and spacing in the y-direction is established. In the second step, each array of Cu-atoms nucleates into a line of weakly spaced Cu-np's and Δx , the spacing in the x-direction, is established.

5.4 Conclusion

Understanding why arrays of Cu atoms aligned with armchair directions are energetically favored over other arrangements is essential for modeling the formation of Cu-np superlattices in terms of the subsequent nucleation of each one of these atomic arrays into a line of metallic particles. In this chapter, results of computer simulations for different distribution settings are presented, we adopted a Cu:C area ratio of 1:8, consistent with a uniform 0.7-nm layer of Cu, to perform calculations based on a numerical model (see experimental details) which assumes modified tight-binding parameters. This is broadly consistent with the results of Zhou et al. [3] for arrays of alkali atoms. Quantification of the formation energies for uniform distributions and arrays of Cu atoms along either the armchair or zigzag direction of graphene suggests that armchair arrays are the more energetically favourable configuration. This confirmed the speculation that, at the longest annealing times, when multiple lines of Cu-np's tend to coalesce, they are typically parallel to an armchair edge and intersect at an angle of 120° .

5.5 References

- [1] A. Akbari-Sharbaf, *Defect-Related Magnetic and Electronic Properties of Graphene*. Diss. The University of Western Ontario, **2014**.
- [2] A. Akbari-Sharbaf, S. Ezugwu, M. S. Ahmed, M. G. Cottam, and G. Fanchini, *Carbon*, **2015**, 95, 199-207.
- [3] J. Zhou, S. Zhang, Q. Wang, Y. Kawazoe and P. Jena, *Nanoscale* **2015**, 7, 2352.

Chapter 6

6 Conclusion

We demonstrated that solution-processed graphene thin films offer a unique platform for the formation of copper nanoparticle superlattices, with parallel lines of Cu-np's that preferentially self-assemble along the armchair crystallographic direction of graphene [1]. An essential component of our superlattice fabrication process is the deposition of ultrathin Cu layers by thermal evaporation and their subsequent annealing and manipulation in an inert atmosphere (e.g. nitrogen) without intermediate exposure to air. Our theoretical calculations suggest that Cu-np arrays tend to form due to the combined minimization of surface and interface energies between graphene and the overlying metal system. At the optimal formation conditions for these superlattices, which correspond to approximately 360°C and 8 h annealing time, superlattices are formed by lines of weakly spaced ($\Delta x \sim 101$ nm) Cu-np's with significantly larger ($\Delta y \sim 102$ nm) interline spacing. These values of Δy , of the same order of magnitude of the wavelengths of visible light, suggested that our systems possess evanescent waveguiding properties for light propagating parallel to the Cu-np's lines. We have demonstrated waveguiding properties using three-dimensional scanning near-field optical microscopy [2], which indicates that our Cu-np's superlattices on graphene are potentially suitable for the fabrication of nano-phonic waveguiding devices. Not only is our superlattice fabrication method suitable to produce Cu-np arrays, but is general enough to be used with a large variety of other metals that weakly bond to graphene (e.g. Au) [3]. Other future applications of our work may stem from the extension of this fabrication method to additional three-dimensional materials different from graphene, as well as the additional optimization of the growth conditions and the fine adjustment of the superlattices parameters. Such future work may broaden the applications of self-assembled metallic superlattices on two-dimensional thin films of graphene and other materials in light trapping devices, magnonic crystals, plasmonic enhancers, and others [4].

6.1 References

- [1] T. Ouyang, A. Akbari-Sharbaz, J. Park, R. Bauld, M. G. Cottam and G. Fanchini, *RSC Adv.*, **2015**, 5, 98814-98821.
- [2] S. Ezugwu, H. Ye and G. Fanchini, *Nanoscale*, **2015**, 7, 252.
- [3] G. Giovannetti, P. A. Khomyakov, G. Brocks, V. M. Karpan, J. Van den Brink and P. J. Kelly, *Physical Review Letters*, **2008**, 101, 026803.
- [4] S. Mokkaati, F. J. Beck, A. Polman, and K. R. Catchpole, *Applied Physics Letters*, **2009**, 95, 053115.

Curriculum Vitae

Name: Tianhao Ouyang

Post-secondary Education and Degrees: Guangdong University of Technology
Guangzhou, Guangdong, China
2010-2014 B.Eng.

Honours and Awards: Students' Comprehensive Performance Scholarship (GDUT)
2012, 2013

Students' Academic Performance Scholarship (GDUT)
2012-2013

Related Work Experience Teaching Assistant
The University of Western Ontario
2014-2016

Publications:

Ouyang, T., Akbari-Sharbaz, A., Park, J., Bauld, R., Cottam, M. G., & Fanchini, G.; Self-assembly metallic nanoparticle superlattices on large-area graphene thin films: growth and evanescent waveguiding properties, *RSC Adv.*, 2015, **5**, 98814-98821.

Bazylewski, P., Akbari-Sharbaz, A., Ezugwu, S., **Ouyang, T.**, Park, J. & Fanchini, G. Graphene thin films and graphene decorated with metal nanoparticles. In Pietro Mandracci (Ed.), *Crystalline and Non-crystalline solids*, 2016, InTech.